https://doi.org/10.5194/egusphere-2026-1481
Preprint. Discussion started: 26 May 2026

Meridional heat transport in the North Atlantic: Effects of ocean and atmosphere grid resolutions in FOCI-OpenIFS-AGRIF 3.0

Sayantani Ojha[1], Joakim Kjellsson[2], Torge Martin[1], Léon Chafik[3], Eric Maisonnave[4], and Wonsun Park[5,6]

[1]GEOMAR Helmholtz Centre for Ocean Research Kiel, Kiel, Germany
[2]Rossby Centre, SMHI, Norrköping, Sweden
[3]Department of Meteorology and Bolin Centre for Climate Research, Stockholm University, Stockholm, Sweden
[4]LOCEAN-IPSL, Sorbonne Université, Paris, France
[5]Center for Climate Physics, Institute for Basic Science (IBS), Busan, Republic of Korea
[6]Department of Integrated Climate System Science, Pusan National University, Busan, Republic of Korea

Correspondence: Sayantani Ojha (s.ojha@geomar.de)

Abstract. We present results of a new coupled climate model configurations named FOCI-OpenIFS-AGRIF 3.0. Advancing from the Flexible Ocean and Climate Infrastructure version 1 (FOCI1, Matthes et al., 2020), the new configuration employs the OpenIFS atmosphere model for improved computational scaling at high grid resolutions. Moreover, a novel coupling technique is developed to enable direct exchange of surface fluxes between an embedded zoom in the ocean model (AGRIF) and the atmosphere component through the coupler in addition to the coupling between the global atmosphere and global ocean. We discuss major differences between three configurations: one with low resolution in ocean (1/2°, 25–50 km) and in atmosphere (∼100 km), one with the refined 1/10° (5–10 km) ocean grid in the North Atlantic but still low resolution atmosphere, and a third one with additionally globally enhanced atmosphere resolution at ∼31 km and 50% more vertical levels. The regionally eddy-rich ocean yields an improved North Atlantic Current path and enhanced northward volume and heat transport simulating a stronger subpolar gyre. Increasing the atmospheric resolution to better match the refined ocean grid yields larger winter heat loss over the subpolar North Atlantic thereby reducing the ocean heat transport into the Nordic Seas despite an unaltered volume transport compared to the configuration with only enhanced ocean resolution. We conclude that just increasing ocean grid resolution shifts meridional heat transport from the atmosphere to the ocean in the North Atlantic region. For a realistic balance between ocean and atmosphere transport matching grid resolutions are required to properly simulate heat exchange at subpolar latitudes.

1 Introduction

The Atlantic meridional overturning circulation (AMOC) is a key player in the global redistribution of heat, freshwater, carbon and nutrients. The AMOC transports warm and saline waters to the subpolar North Atlantic where the heat is ventilated to the atmosphere and upper ocean waters are transformed into North Atlantic Deep Water (NADW). The AMOC carries almost 1.2 PW of heat northward at 26.5°N which is 60% of the net poleward heat flux carried by the global oceans (Ganachaud and Wunsch, 2000; Trenberth and Fasullo, 2017). The northward heat transport is an crucial contribution by the global overturning

https://doi.org/10.5194/egusphere-2026-1481
Preprint. Discussion started: 26 May 2026

circulation to regional climate and its variability. Many oceanic and atmospheric processes contribute to the meridional heat transport (MHT) in the North Atlantic ranging from the sensible and latent surface heat fluxes to basin-scale overturning and gyre circulation to mesoscale dynamics, including eddies.

The MHT in the North Atlantic has been estimated in many previous studies by using surface heat fluxes or in situ measurements. Hsiung (1985) computed the MHT as the transport required to balance air–sea heat flux observations and Trenberth and Caron (2001) calculated it as the the residual from the top-of-atmosphere radiation balance that is unexplained by atmospheric transport. Argo floats (Hobbs and Willis, 2012) as well as ship-borne instruments (Hall and Bryden, 1982; Koltermann et al., 1999; Talley, 2003) have also been used to measure the MHT. In recent decades moorings of the Rapid Climate Change-Meridional Overturning Circulation and Heatflux Array (RAPID-MOCHA) are providing continuous measurements of MHT at 26.5°N (Johns et al., 2011; Moat et al., 2022) and the Overturning in the Subpolar North Atlantic Program (OSNAP, Lozier et al., 2019) provides observational MHT data for the subpolar gyre region. However in situ measurements at a given latitude cannot result in a robust MHT variability as it can not capture the mesoscale activities realistically which are essential for the Atlantic MHT estimation.

It is essential for numerical ocean models to realistically represent mesoscale eddies, either by explicitly resolving them or through appropriate parameterization, to effectively replicate the ocean's dynamic response. In order to produce the correct transfer of kinetic energy between large scales and mesoscale eddies, the ocean model should be able to resolve the Rossby radius (Kjellsson and Zanna, 2017). Non-eddying ocean models, often use an eddy-parameterisation scheme such as the Gent–McWilliams (GM, Gent and Mcwilliams, 1990) method to account for unresolved eddy processes, which however does not include the kinetic energy transfer accurately. As a result, the models with low horizontal resolution show biases in the dynamics of the Gulf Stream, the Kuroshio Current and the Antarctic Circumpolar Current.

An accurate representation of the western boundary currents, such as the Gulf Stream in the North Atlantic and the Kuroshio in the North Pacific, is crucial for better understanding ocean-atmosphere interactions and their impact on climate (Minobe et al., 2008; Ma et al., 2016; Griffies et al., 2015; Renault et al., 2016; Omrani et al., 2019). A realisitc representation of the Gulf-Stream extension leads to improvements in sea surface temperatures (SSTs) and air–sea heat fluxes around this region (Bryan et al., 2007; Small et al., 2014; Bellucci et al., 2021; Athanasiadis et al., 2022). Marzocchi et al. (2015) and Martin and Biastoch (2023) achieved significant improvements of the North Atlantic Current (NAC) and the Gulf-Stream separation already with a 1/12° and 1/10° ocean grid, respectively. They have also found improvements in the representation of boundary currents, depth of winter mixing in the Labrador Sea, and the transport of overflows at the Greenland–Scotland Ridge. Multiple studies have shown that an increased ocean model horizontal resolution tends to simulate a stronger and more realistic mean subpolar gyre and AMOC (Hirschi et al., 2020; Roberts et al., 2020; Meccia et al., 2023) which further enhance the poleward heat transport which improves simulation of the mean SSTs, sea surface salinity, and sea ice cover in the high-latitude North Atlantic (Grist et al., 2018; Menary et al., 2018; Docquier et al., 2019).

There is a general agreement that eddy-rich models produce a more realistic North Atlantic climate than non-eddying and eddy-permitting models (Marzocchi et al., 2015; Roberts et al., 2020; Sieker et al., 2026). However, eddy-rich models come at a high computational cost due to finer horizontal resolution, which demands a shorter time step, and is often accompanied by

https://doi.org/10.5194/egusphere-2026-1481
Preprint. Discussion started: 26 May 2026

enhanced vertical resolution. To fully benefit from such expensive simulations, output is stored at a higher frequency, which is demanding on I/O and disk space. Thus, eddy-rich model simulations exceeding a couple of centuries are rare. To overcome this limitation, an alternative in ocean modelling is to nest a high-resolution regional domain into a global base model at coarser resolution (Biastoch et al., 2018). With two-way interaction enabled, nested models still enable far-field feedbacks of the regional mesoscale processes, which can be identified and quantified by either altering nest sizes (Biastoch et al., 2008b) or by running parallel studies using the same base model without nest (Biastoch et al., 2008a). The improvement of the climate mean state by including an eddy enabling nested ocean model in a coupled climate model has been demonstrated by Matthes et al. (2020), who found a reduction in the prominent North Atlantic cold bias, an improvement in the North Atlantic Current path and a more realistic Gulf Stream separation.

Another methodology, which employs unstructured meshes (Wang et al., 2008; Ringler et al., 2013; Sidorenko et al., 2015) is also considered to be highly efficient in mitigating computational constraints. In this approach high resolution is applied to dynamically active regions while retaining a relatively coarse resolution elsewhere. For example, the Alfred Wegener Institute Climate Model (AWI-CM) with a sea ice-ocean component based on an unstructured mesh simulates a more realistic climate mean state than the average of five well-established Coupled Model Intercomparison Project Phase 5 (CMIP5, Wuebbles et al., 2014) models (Sidorenko et al., 2015). Moreover, Rackow et al. (2018) showed that this model yields internal variability largely consistent with observations.

In this study we discuss the implications of enhancing ocean and atmosphere model grid resolutions on ocean large-scale circulation, surface fluxes and meridional heat transport in the context of climate mean state simulations. For this we compare three different coupled model configurations with a focus on the North Atlantic region. The reference, low-resolution configuration features a non-eddying ocean system and the two high-resolution configurations run with strongly eddying North Atlantic, where one of these also features matching high-resolution in the atmosphere. The main questions we address are: (1) How does hydrography and atmospheric temperature over the North Atlantic region change with enhanced grid resolutions? (2) How is this connected to large-scale ocean circulation changes? (3) How do these responses affect the mean state meridional heat transport in ocean and atmosphere?

2 Data and Methodology

2.1 Model description

The FOCI-OpenIFS model is based on the Flexible Ocean and Climate Infrastructure version 1 (FOCI1, Matthes et al., 2020), but uses the Open Integrated Forecasting System (OpenIFS) atmosphere model instead of the European Centre Hamburg Model, 6th generation (ECHAM6, Stevens et al., 2013). The OpenIFS model was chosen over ECHAM6 (Stevens et al., 2013) due to the better scalability of the former at high horizontal resolutions. The ocean component, the Nucleus for European Modelling of the Ocean (NEMO, Madec, 2016), is described briefly in section 2.1.2 as it it largely the same as in FOCI1. Most importantly, FOCI-OpenIFS shares the capability to regionally refine the ocean grid by two-way nesting. However, a

https://doi.org/10.5194/egusphere-2026-1481
Preprint. Discussion started: 26 May 2026

novel coupling technique was developed and is first described here in section 2.1.3. For further details the reader is referred to (Matthes et al., 2020).

2.1.1 Atmosphere and Land

The OpenIFS atmosphere model is based on the forecast model from the European Centre for Medium-Range Weather Forecasts (ECMWF) Integrated Forecasting System (IFS) cy43r3 (Temperton et al., 2001; Hortal, 2002). The low-resolution simulation uses the O96 reduced octahedral Gaussian grid and $T_{co}95$ cubic spectral truncation (≈ 100 km) with 91 vertical hybrid levels and a 1800 s time step, while the high-resolution simulation uses the O320 grid and $T_{co}319$ spectral truncation (31 km) with 137 vertical levels and 900 s time step. The low-resolution configuration is the same as used by Savita et al. (2024). Only one namelist parameter is changed between the low-resolution and high-resolution configurations: the time step is changed from 1800 s to 900 s. This follows recommendations from ECMWF. Other parameter changes such as diffusion coefficients, gravity-wave drag parameters, etc are changed internally in the model as function of grid resolution. In particular, we note that the radiation call frequency is changed from 3 hours in low resolution to 1 hour at high resolution.

Land-surface calculations are done by the Hydrology Tiled ECMWF Scheme for Surface Exchanges over Land (HTESSEL, Balsamo et al., 2009) module included in OpenIFS. Vegetation types and albedo over snow-free surfaces are prescribed from climatology. All air-sea fluxes are calculated by OpenIFS and then passed to the ocean/sea-ice model.

In all experiments the Charnock coefficient is constant, 0.018. Wind stress is calculated by the surface module in OpenIFS as

$$(\tau_x, \tau_y) = \kappa\rho\sqrt{C_m}\sqrt{u_s^2 + v_s^2}(u_s, v_s), \tag{1}$$

where $\mathbf{u}_s = (u_s, v_s)$ is the near-surface horizontal wind, ρ is air density, $\kappa = 0.4$ is the von Karman constant and C_m is a drag coefficient which in dependent on atmospheric stability. Hence, our simulations will not include the so-called "eddy killing" effect (Zhai et al., 2010), where wind stress induces a torque opposite of the rotation of mesoscale ocean eddies.

2.1.2 Ocean and sea ice

We use the ocean–sea ice model of FOCI1.0 (Matthes et al., 2020), which is NEMO version 3.6 (Madec, 2016) and Louvain-la-Neuve Sea Ice Model version 2 (LIM2, Fichefet and Maqueda, 1997), and also the same tripolar global grid ORCA05 with 46 vertical z-star levels and partially filled bottom cells. The ORCA05 grid has a nominal resolution of 0.5° (nominal grid spacing of 50 km, converges to 25 km in Nordic Seas) and thus does not permit explicitly resolved mesoscale eddies, i.e. this configuration is considered "non-eddying". Instead, mixing of tracers by mesoscale eddies is parameterized (Treguier et al., 1997) with the eddy diffusivity capped at $1000\ \mathrm{m^2\ s^{-1}}$.

Sea-ice dynamics and physics is done by the LIM2 sea-ice model (Fichefet and Maqueda, 1997) which uses the same horizontal resolution as the ocean model but on a B-grid instead of the C-grid of the ocean. The sea-ice model call is every 10 mins in the Adaptive Grid Refinement In Fortran (AGRIF, Debreu and Blayo, 2008) compared to 1 hour in ORCA05 to avoid Courant-Friedrichs-Lewy (CFL) violations. Bare sea-ice albedo is set to a fixed α_{ice}. We use only one thickness category.

https://doi.org/10.5194/egusphere-2026-1481
Preprint. Discussion started: 26 May 2026

We apply two-way nesting using AGRIF (Debreu and Blayo, 2008) to enhance the grid resolution from $0.5°$ to $0.1°$ over the entire subpolar North Atlantic region from 30° to 85°N. With a grid spacing of $<$10 km (converging to 5 km around Greenland), this nested regional model called VIKING10 enables a strongly eddying representation of the Gulf Stream and North Atlantic Current—thereby mitigating the prominent North Atlantic cold bias—and also improved boundary currents at higher latitudes (Matthes et al., 2020; Martin and Biastoch, 2023). The nested ocean–sea ice model is fully coupled to the global climate model as in FOCI1 but uses a more sophisticated coupling method as described below.

To accommodate the higher horizontal resolution the nest uses a shorter time step, smaller coefficients for horizontal viscosity and tracer diffusion, and the parametrisation of mesoscale eddy tracer fluxes is turned off. We reduce the coefficients for horizontal viscosity, $A_{\mathrm{h,m,0}}$, and tracer diffusion, $A_{\mathrm{h,t,0}}$ from the ORCA05 to the VIKING10 grid as a function of horizontal resolution following

$$A_{\mathrm{h,m,0}} = A_{\mathrm{h,m,0}} \left(\frac{\Delta_{\mathrm{nest}}}{\Delta_{\mathrm{ORCA05}}} \right)^3 \text{ and} \tag{2}$$

$$A_{\mathrm{h,t,0}} = A_{\mathrm{h,t,0}} \frac{\Delta_{\mathrm{nest}}}{\Delta_{\mathrm{ORCA05}}}, \tag{3}$$

where Δ_{nest} and Δ_{ORCA05} are the grid spacing of the nest and global ORCA05 grids, respectively. We applied and AGRIF refinement factor of $\frac{\Delta_{\mathrm{nest}}}{\Delta_{\mathrm{ORCA05}}} = 5$. Hence, horizontal diffusion is reduced by a factor 5 and horizontal viscosity by a factor 125 (Table 1).

The ocean component NEMO simulates the global ocean on the ORCA05 grid and sends/receives fluxes to/from OpenIFS. Over the nest, AGRIF simulates the North Atlantic using boundary conditions from the global ORCA05 grid and also sends/receives fields to/from OpenIFS independently of the global ORCA05 grid. The 3D fields of velocity and tracers from AGRIF are used to update the global model over the North Atlantic every three nest time steps, i.e. every 30 minutes.

We note that our version of NEMO 3.6 was modified to (i) send the AGRIF mask to the OASIS coupler (see coupling method below), (ii) remove checking of coupling frequency since it is different for NEMO and AGRIF, (iii) avoid calling the `oasis_enddef` in NEMO but instead in the last AGRIF definition. The last two code modifications are available in later releases of NEMO.

2.1.3 Coupling

In FOCI verison 1.0 (Matthes et al., 2020), the coupler only sends and receives fields between the ECHAM6 atmosphere and the NEMO global ocean. Coupling fields such as wind stress, evaporation and heat flux from ECHAM6 are computed based on ORCA05 surface state, then written to a netCDF file on disk and finally read and remapped to the AGRIF grid. There are several disadvantages with this method. First, from a computational point of view, reading and writing from/to disk is much slower than direct communication between model components via Message-Passing Interface (MPI). In addition, the "file-based" coupling was found to fail on some HPCs due to issues with the netCDF library when a file is kept open and its data is replaced multiple times. Second, the coupling exchange via the ocean parent grid imposes the combination of two spatial interpolations, thus combined smoothing, on top of the zoom area, (i) between the NEMO child and parent grids, via internal AGRIF-NEMO

https://doi.org/10.5194/egusphere-2026-1481
Preprint. Discussion started: 26 May 2026

exchanges, and (ii) between the NEMO parent grid and the OpenIFS grid. Therefore, we implemented direct coupling between the AGRIF nest and the OpenIFS atmosphere as a novelty to FOCI-OpenIFS. The surface fluxes calculated by OpenIFS make full use of the surface state over the high-resolution nest which is particularly important when the atmosphere grid is finer than the ORCA05 grid, i.e. when coupling the O320 ($T_{co}319$) grid to the nest. Furthermore, performing all coupling via Ocean Atmosphere Sea Ice Soil - Model Coupling Toolkit (OASIS3-MCT v5) (Craig et al., 2017) rather via file I/O alleviates a possible performance bottleneck.

In principle, coupling the OpenIFS atmosphere to both global NEMO and AGRIF means we couple the atmosphere to two separate ocean grids simultaneously even if both grids exist in the same executable. A detailed description of the coupling method can be found in Maisonnave (2019). Note that OpenIFS only sends fields to the OASIS coupler once per model time step and the fields are then sent from OASIS to both NEMO and AGRIF. Hence, the surface fluxes sent to OASIS are identical but they are different when received by NEMO and AGRIF due to differences in interpolation. OASIS sends NEMO global and AGRIF nested surface state to OpenIFS which then blends the two. For example, SST in OpenIFS is set to

$$\mathrm{SST}_{\mathrm{atm}}(x,y) = (1 - M_{\mathrm{atm}}(x,y))\ \mathrm{SST}_{\mathrm{glo}}(x,y) + M_{\mathrm{atm}}(x,y)\ \mathrm{SST}_{\mathrm{agr}}(x,y), \tag{4}$$

where $\mathrm{SST}_{\mathrm{glo}}$ and $\mathrm{SST}_{\mathrm{agr}}$ are SST from NEMO parent and AGRIF child grids, respectively, interpolated to the OpenIFS grid by OASIS. M_{atm} is a mask on the OpenIFS grid with value 1 inside the AGRIF nest and 0 elsewhere (Fig. 1a) with a transition zone on the AGRIF zoom boundary. The mask with transition zone, M_{agr}, is built on the child grid in AGRIF. The value is then interpolated on the global atmosphere grid and sent as coupling field to OpenIFS as M_{atm}, where it is used following the above formula. The parent grid, i.e. global NEMO, constructs the mask, M_{agr}, which is then sent as coupling field to OpenIFS as M_{atm} and the remapping is handled by OASIS. The same method is used for sea-ice concentration and other ocean surface fields. A similar mask is also sent to the river routing scheme, M_{rnf}, so that AGRIF only uses river input over the AGRIF domain. The method allows the user to construct and couple multiple AGRIF nests, e.g. an AGRIF nest within another AGRIF nest such as the INALT60 nest (Schwarzkopf et al., 2019), but this has not been tested.

Since the NEMO and AGRIF grids have different resolutions, the OASIS remapping options for atmosphere fluxes differ for the two grids. For OpenIFS-NEMO remapping we use Gaussian weights with 9 neighbours and a weight of 2.0. For OpenIFS-AGRIF remapping we use Gaussian weights with 15 neighbours and 0.1 weight. This was done to minimise the interpolation error (Maisonnave, 2021).

2.1.4 River routing

We use a simple river routing scheme where surface and sub-surface runoff from HTESSEL is binned into river basins and scattered to river mouths on the ORCA05 grid. The global gathering and scattering is done such that the volume flux is conserved for each river. River runoff from the runoff mapper is remapped to the NEMO and AGRIF grids using the `LOCCUNIF` method which was ported from OASIS3-MCT v5 to our version. Each river mouth is remapped to 4 neighbouring grid cells on the ORCA05 grid and 12 grid cells on the AGRIF grid.

https://doi.org/10.5194/egusphere-2026-1481
Preprint. Discussion started: 26 May 2026

Table 1. Model simulations used in this study. For the global ocean model the ORCA05 grid is used, the regional nest uses a factor 5 refinement thereof. Iso-neutral tracer diffusivity is $A_{\mathrm{h,t}}$ and iso-level bi-Laplacian viscosity is $A_{\mathrm{h,m}}$.

	LL	LH	HH
Atmosphere Δx	100 km	100 km	31 km
Atmosphere Δt	1800 s	1800 s	900 s
Ocean (global) Δx	0.5°	0.5°	0.5°
Ocean (global) Δt	1800 s	1800 s	1800 s
Ocean (global) $A_{\mathrm{h,t}}$	600 $\mathrm{m^2\ s^{-1}}$	600 $\mathrm{m^2\ s^{-1}}$	600 $\mathrm{m^2\ s^{-1}}$
Ocean (nest) Δx	N/A	0.1°	0.1°
Ocean (nest) Δt	N/A	600 s	600 s
Ocean (nest) $A_{\mathrm{h,m,0}}$	N/A	$-2.4 \cdot 10^{10}$ $\mathrm{m^4\ s^{-1}}$	$-2.4 \cdot 10^{10}$ $\mathrm{m^4\ s^{-1}}$
Ocean (nest) $A_{\mathrm{h,t,0}}$	N/A	120 $\mathrm{m^2\ s^{-1}}$	120 $\mathrm{m^2\ s^{-1}}$

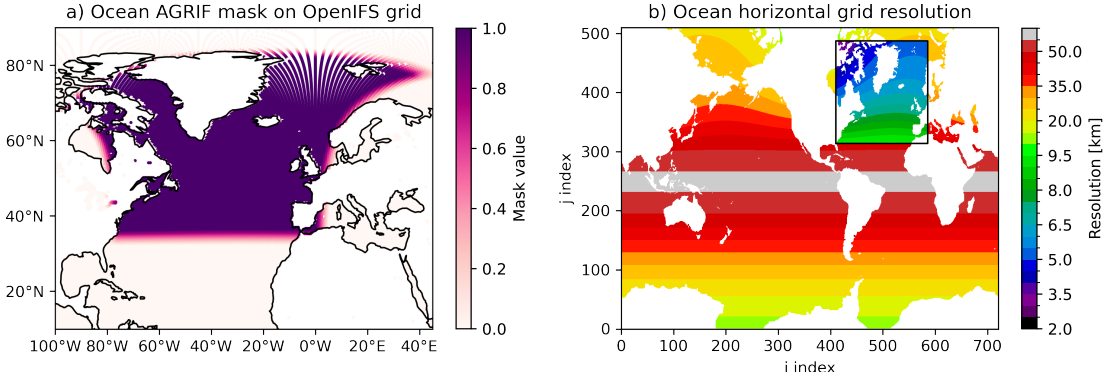

Figure 1. (a) Mask identifying the nested ocean region on the atmosphere grid O320 in the OASIS coupler highlighting the transition zone between AGRIF nest (mask=1) and global base model (mask=0). (b) The horizontal resolution, $\Delta = (\Delta x + \Delta y)/2$, on the ORCA05 and VIKING10 grids in NEMO.

2.2 Simulations

Since FOCI-OpenIFS comprises the OpenIFS atmosphere and the NEMO ocean model it shares many similarities with other climate models such as European Consortium Earth System Model (EC-Earth, Hazeleger and Bintanja, 2012), Centre National de Recherches Météorologiques Coupled Model, version 6 (CNRM-CM6, Sérazin et al., 2015) as well as the ECMWF-IFS simulations for the High-Resolution Model Intercomparison Project (HighResMIP, Roberts et al., 2018). A technical comparison can be found in (Kjellsson et al., 2020). The FOCI-OpenIFS model is distinct from these models by being the only one using two-way nesting in NEMO with AGRIF.

https://doi.org/10.5194/egusphere-2026-1481
Preprint. Discussion started: 26 May 2026

Key model parameters for each simulation are listed in Table (1). We have performed three simulations by using different atmosphere and ocean resolutions: LL, LH and HH where LL denotes low-resolution atmosphere ($T_{co}95$) and non-nested ocean (ORCA05), LH is low-resolution atmosphere and nested ocean (ORCA05-VIKING10), and HH is high-resolution atmosphere and nested ocean (Table 1, Fig. 1b). We recognise that the models will continue to drift over time, due to the short spin-up, we have used the difference between the different configurations as an estimate of the impact of changing resolution on the atmosphere and ocean responses assuming a common drift in all simulations.

All the experiments have carried out for 100 years by using control-1950 forcing with external forcings fixed at 1950 values. Since the model drift is considerably reduced after around year 50 our analysis is focused on the last 50 years (mostly annual mean) of each simulation.

The SST and sea-surface salinity (SSS) biases at the end of control-1950 period (averaged over years 51–100) over the North Atlantic Ocean are shown in Fig. 2 for each model resolution. A common feature across the model resolutions is a cold and fresh bias in the central subpolar North Atlantic which is also a feature found in many climate (Kuhlbrodt et al., 2018; Roberts et al., 2019) models. A similar bias is also reported in Matthes et al. (2020) and improved significantly by implementing the ocean nesting. The impact of the nested ocean is discussed in details in the next sections. The high resolution atmosphere shows much reduced bias in SST compared to LL. It is very evident from this figure that the higher resolution in both atmosphere and ocean have improved the surface bias substantially.

3 Results

In the following we present differences LH−LL for demonstrating the impact of enhancing ocean horizontal grid resolution only, differences HH−LH for the impact of enhanced atmosphere grid resolution (incl. the VIKING10 nest), and differences HH−LL for illustrating the total changes and also for identifying the locally dominant effect. The analysis focuses on the difference of the climate mean state between the three experiments and the differences of 50-year means are displayed if not noted differently.

3.1 Imprints in North Atlantic hydrography and air temperature

For a starting point and as a guiding graphic of the following analysis we present in Fig. 3 annual-mean temperature and salinity differences zonally averaged over the North Atlantic basin (limited to 60°W–0 in the atmosphere). Three major differences are apparent immediately when introducing eddying resolution to the ocean (LH−LL): the surface and upper ocean warms (and becomes saltier) between 45°N and 65°N, the ocean at mid-depth and 10-–45°N cools (and freshens) and the atmosphere north of 45°N warms. Increasing both horizontal and vertical resolution of the global atmosphere from LH to HH introduces a widespread cooling in the troposphere, except for a warming at 400–200 hPa north of 50°N. This cooling extends into the ocean, but as a weaker signal. In total (HH−LL), atmospheric warming and cooling compensate mostly resulting in a weak warming but a distinct cold signal over the Nordic Seas.

https://doi.org/10.5194/egusphere-2026-1481
Preprint. Discussion started: 26 May 2026

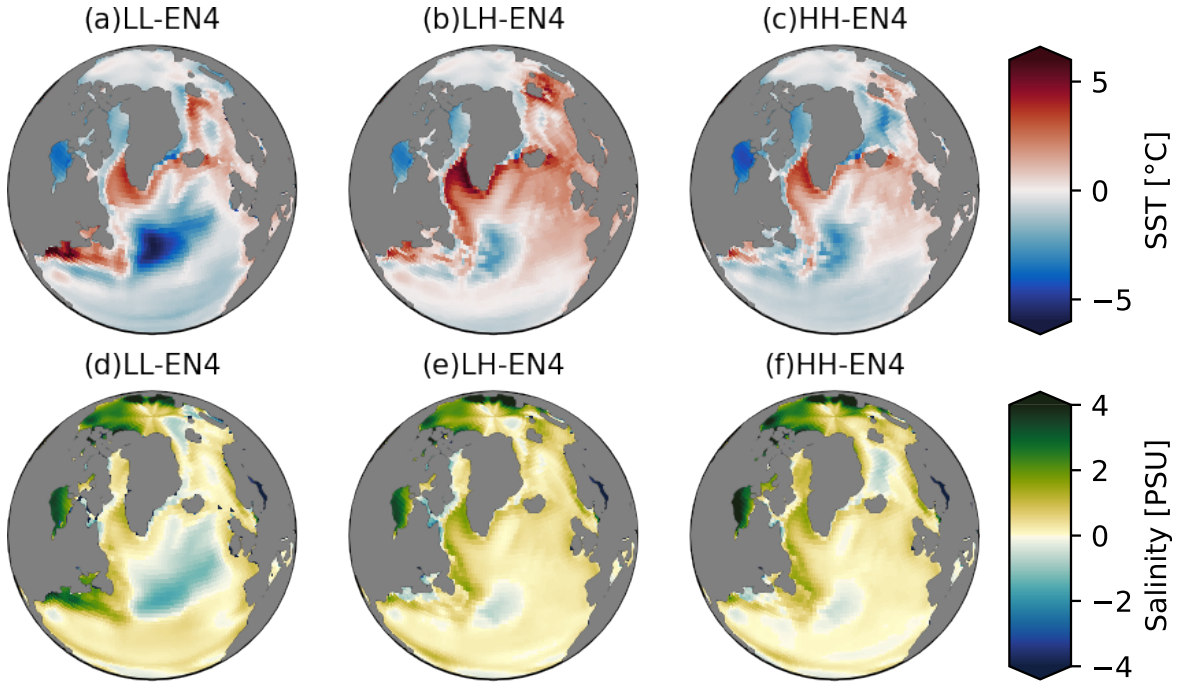

Figure 2. For the three simulations (LL, LH, and HH), (a-c) the annual mean bias in SST (°C), and (d-f) SSS (PSU) with respect to the EN4 dataset (Good et al., 2013). The differences are computed over simulations years 51–100, the EN4 averages are based on years 1973-2022.

The simulations with ocean nest, LH and HH, feature a significantly warmer upper ocean at mid- and subpolar latitudes than LL. This significant warming is prominently seen in SST differences (Fig. 4a, b) which is strongest in the path of the NAC and along the western boundary of the North Atlantic basin. Regional negative differences in SST are present in the central Labrador and Irminger Seas and, more strongly, in the Nordic Seas. Both regional cold signals are more pronounced in HH−LL than LH−LL and linked to changes in open ocean deep convection as further discussed below.

In contrast to the basin-scale SST warming at subpolar latitudes, implementing VIKING10 causes colder mid-depth ocean temperatures at mid- to sub-tropical latitudes (Fig. 4d, e). A significant reduction in potential temperature is found at depths between 500 and 1500 m, with the most pronounced cooling occurring around 800 m depth. The horizontal distribution of this cold signal between 500 m and 1000 m (Fig. 4) spreads across the entire basin filling the subtropical gyre and extends northward to 45°N. Notably, salinity changes are well aligned with the temperature difference. In the nested simulation, salinification accompanies surface warming, while a significant freshening is observed in the mid-depth ocean, where a cooling is found.

The noticeably cooler atmospheric temperatures of HH (Fig. 3b) are likely due to the cloud radiative forcing. We did not tune HH specifically to the enhanced resolution but rather kept most parameters as similar as possible to the low resolution configuration. We found a substantial change between the surface and the top of the atmosphere radiative balances associated with a decrease in overall cloud cover (not shown). This can be explained by the dependency of the cloud erosion rate on the

https://doi.org/10.5194/egusphere-2026-1481
Preprint. Discussion started: 26 May 2026

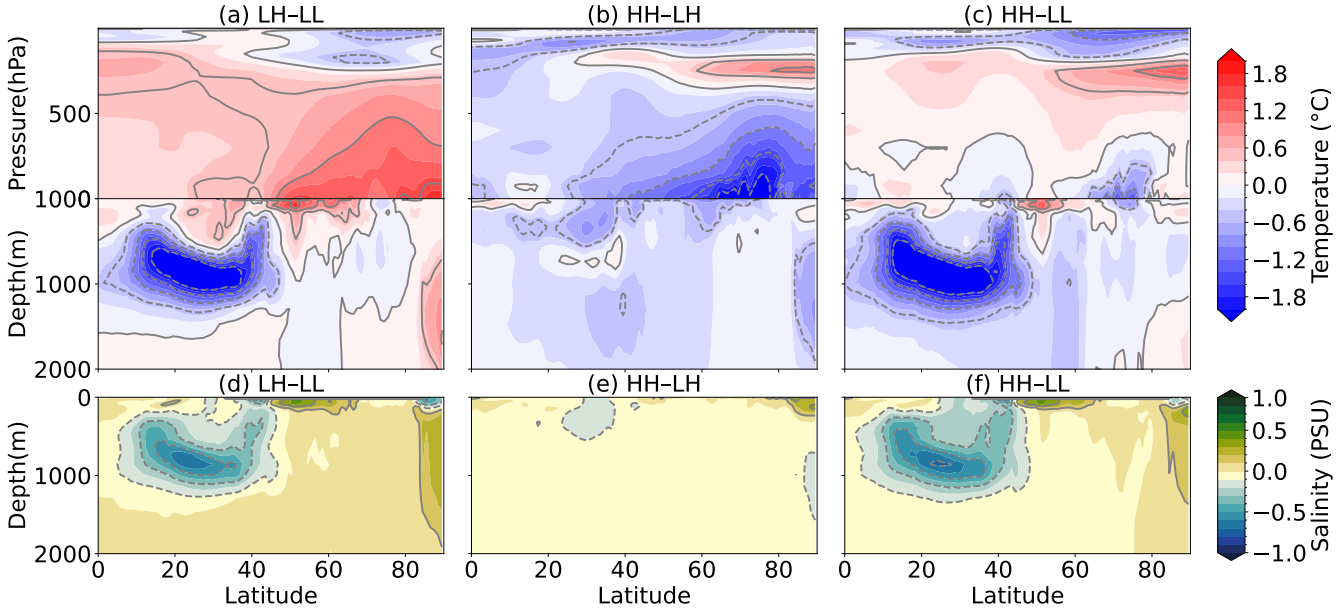

Figure 3. Annual-mean differences in North Atlantic region zonal mean (a–c) air temperature (°C) as well as ocean potential temperature and (d–f) salinity (PSU) between the three model configurations. In the atmosphere the region is limited to 60°W–0°. The differences are computed over simulations years 51–100.

model time step in OpenIFS 43r3. The cloud erosion rate and possibly other cloud parameters would require re-tuning in HH due to the shorter time step (900 s compared to 18000 s in LL), which we did not do. In the Arctic region, the surface cooling is more intense and extends up to the upper-troposphere (400 hPa). In consequence, sea ice is thicker and covers a larger area in the Arctic in HH compared to LH, resulting in lower surface temperatures (Fig. A1). We speculate that the upper tropospheric warming north of 50°N and at about 200 hPa is related to changes in the polar jet and lowering of the tropopause resulting from a vastly colder troposphere in HH.

3.2 Changes in ocean circulation

The implementation of the VIKING10 nest yields a more realistic, less zonal path of the NAC and a stronger subpolar gyre resulting in significant warmer SST and upper-ocean temperature at 45°N–65°N (Fig. 4a–c). This mitigates the prominent and well-known North Atlantic cold bias in LH and HH (Fig. 2a–c) and confirms earlier applications of the VIKING10 nest (Matthes et al., 2020; Martin and Biastoch, 2023). The northward shift of the NAC replaces cold, fresh polar waters with warm, saline subtropical waters in the region of the bias. This ocean dynamics–driven temperature change extends into the atmosphere where it is visible from the surface reaching far up into the troposphere (Fig. 3a). The warmer Atlantic water in LH and HH is associated with reduced sea-ice thickness in the Arctic Ocean (Fig. A1), mostly in LH as HH features an overall cooler climate

https://doi.org/10.5194/egusphere-2026-1481
Preprint. Discussion started: 26 May 2026

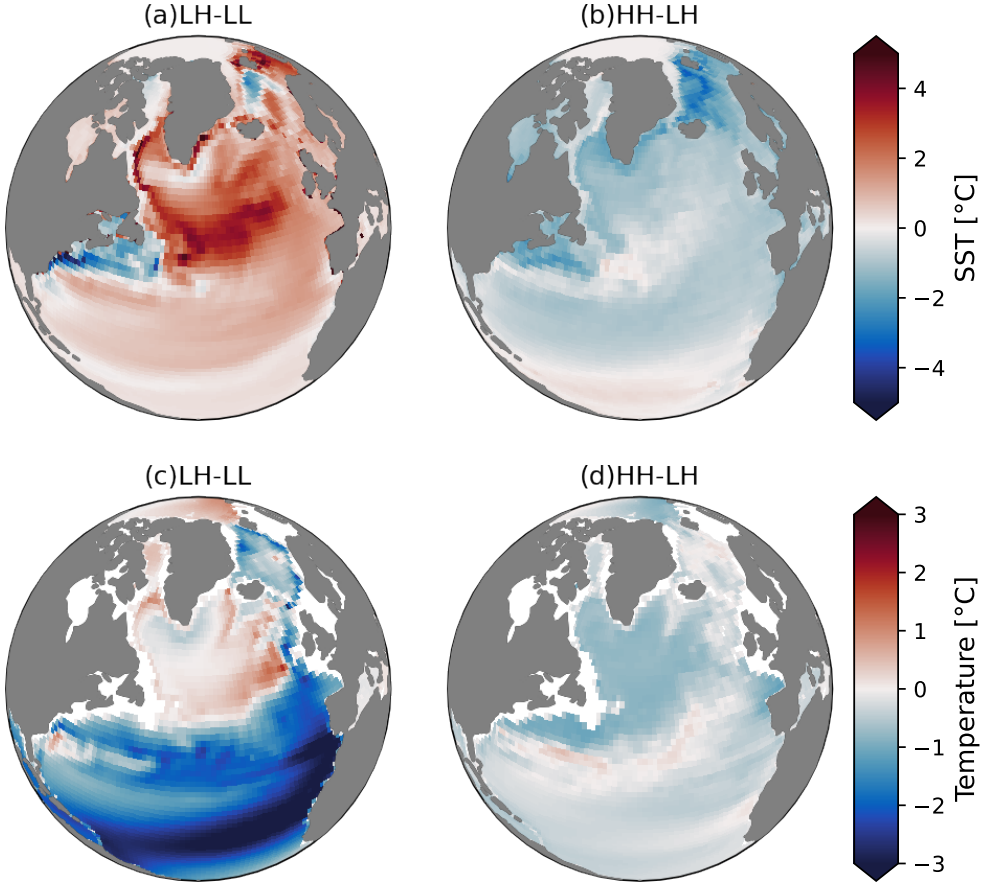

Figure 4. Annual mean differences in (a-b) SST (°C), and (c-d) 500–1000 m mean potential temperatures (°C) between the model configurations, LL, LH, and HH respectively. The differences are computed over simulations years 51–100.

state. We speculate that the thinner sea-ice cover may contribute further to warmer temperatures over Greenland and the Nordic Seas.

We tested various hypotheses to explain the cold and fresh difference at mid-depth of 500–1500 m at mid- to subtropical latitudes in LH−LL. Among those were a larger southward export of cold, fresh polar water by a stronger subpolar gyre, stronger gyre-gyre interaction (mixing across the NAC) and enhanced southward leakage of Arctic-sourced fresh water along the eastern boundary of the basin, and changes in the outflow from the Mediterranean Sea. The hypotheses relating to an altered redistribution and southward export of polar waters originate from differences in passive tracer pathways introduced by VIKING10 as shown in Martin and Biastoch (2023). We found no conclusive evidence for this in our simulations however.

The only robust explanation is to link this difference to substantial changes in Mediterranean outflow water (MOW), which is a prominent warm and saline intermediate-depth water mass of heat and salinity at this latitude in the North Atlantic. A zonal cross-section of temperature through the Gibraltar Strait shows that LH and HH are colder in the area of the MOW than LL (Fig.

https://doi.org/10.5194/egusphere-2026-1481
Preprint. Discussion started: 26 May 2026

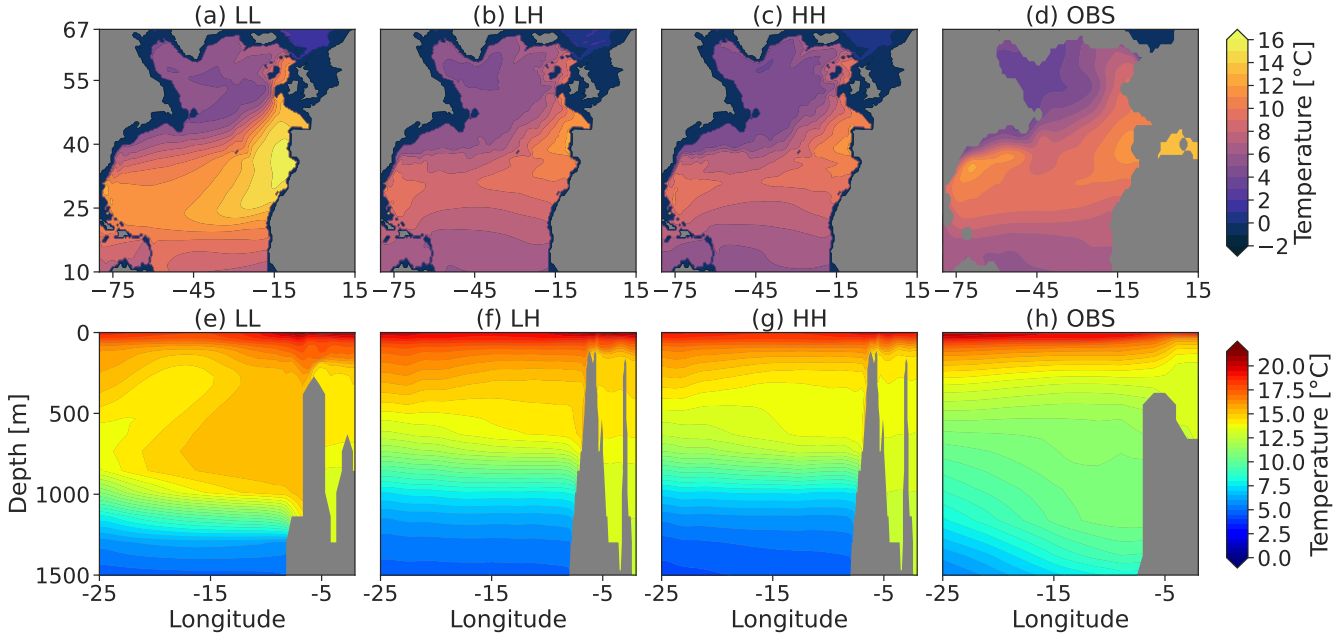

Figure 5. Annual mean temperature (°C) at 800 m depth (a–d), and vertical cross-section of temperature (°C) through the Strait of Gibraltar (36°N) (d–h) for all three simulations and EN4 datasets (Good et al., 2013). The annual means are computed over simulations years 51–100, the EN4 averages are based on years 1973–2022.

5). The same cross section of salinity shows that LH and HH are also fresher than LL in the same region (Fig. A2). Further, the horizontal patterns of 800 m temperature and salinity show pronounced differences in the region of MOW indicating a reduced outflow in LH and HH. The Strait of Gibraltar is included in the VIKING10 nest region and thus its bathymetry is more realistically represented in LH and HH. In LL the strait is wider and deeper—despite a limiter implemented in the NEMO code reducing the north-south grid cell width to 20 km at this location—and thus allows for an unrealistically large outflow (Fig. 5). Although the outflow is reduced with the implementation of the VIKING10 nest and an actual overflow is simulated, the overflow does not reach deep enough to match observations. MOW is observed to spread at a depth 1000–1100 m but the MOW in LH and HH is mixed and entrained more rapidly, equilibrating at shallower depth of around 700 m. This is a common overflow issue in z-layer models, especially with insufficient vertical resolution (Legg et al., 2009). We thus conclude that it is a lack of MOW and more realistic simulation of its spreading in LH and HH that explains the mid-depth, sub-tropical cold and fresh difference.

While the above described circulation changes explain regional differences in hydrography, altogether these also affect the AMOC. The vertical structure of the AMOC in depth coordinates in Fig. 6a reveals a clear strengthening with increasing model resolution. The HH configuration exhibits the strongest overturning circulation, with maximum transport exceeding 20 Sv. In addition, the southward return flow intensifies with resolution, reaching comparable magnitudes in both the LH and HH configurations. Additionally, we show AMOC strength diagnosed as the maximum of the overturning streamfucntion at

https://doi.org/10.5194/egusphere-2026-1481
Preprint. Discussion started: 26 May 2026

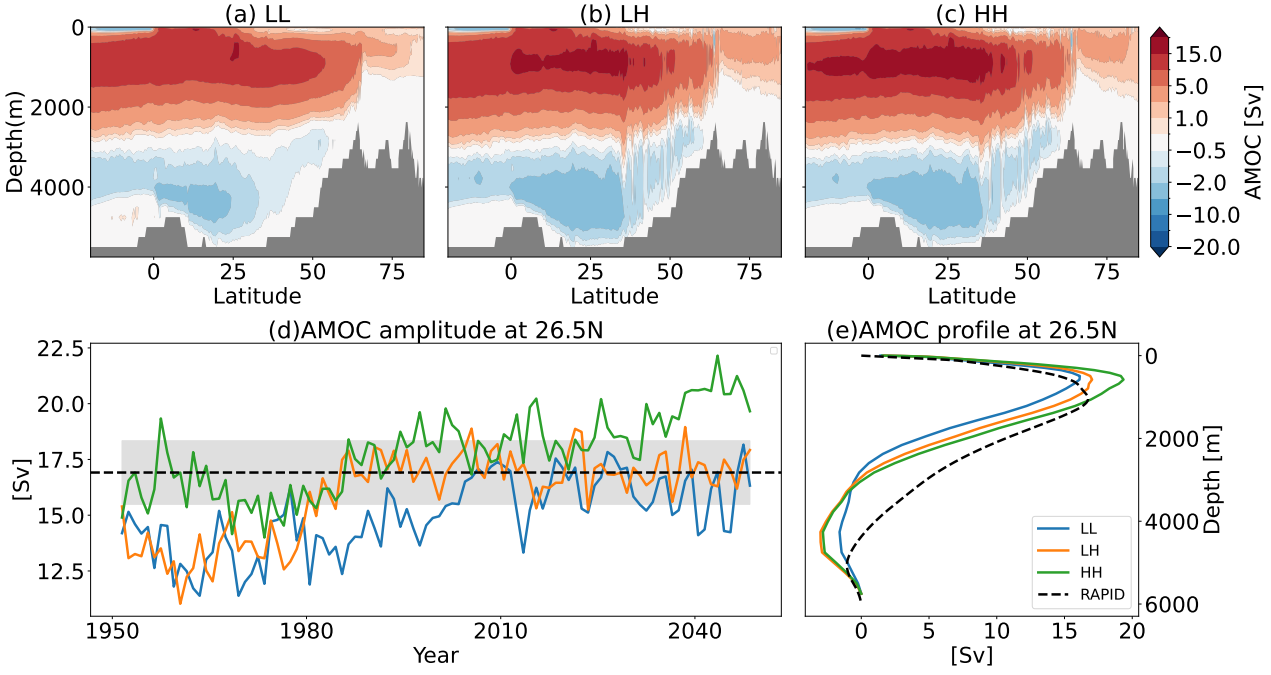

Figure 6. (a-c) Mean Atlantic meridional overturning streamfunction in depth coordinates. The mean is computed over simulations years 51–100 (d) Time series and (e) Vertical profile of maximum AMOC transport (Sv) at 26.5°N. In (d) and (e) an observational AMOC mean strength estimate from the RAPID array is shown as dashed black line; in (d) gray shading also depicts ±1 standard deviation indicating the range of interannual variability of this estimate.

26.5°N and the vertical extent of the overturning cell in Fig. 6b, c. A comparison with the observed transport at the RAPID array indicates that overall the three simulations perform relatively well, starting low but trending towards the observed strength, with LL tending to underestimate AMOC strength and HH to overestimate the transport in the last couple of decades. The depth of the maximum AMOC at 26.5°N is shallower in all three configurations (approximately 800 m) compared to observations. The depth profile of AMOC shows a difference of about 5 Sv between the LL and HH simulations, while the LH configuration exhibits the closest magnitude to the observed transport. This stronger AMOC result from explicitly resolving mesoscale ocean dynamics in VIKING10, which allows for a more accurate representation of the NAC, northward water mass transport, surface heat loss, boundary currents, and downwelling along the shelf slopes, all of which are crucial components of the AMOC. Furthermore, open ocean deep convection in the subpolar North Atlantic region is larger with VIKING10, especially in HH, and will be discussed further below.

A stronger AMOC is an enhanced northward volume transport in the upper ocean in the first place. Since the water mass transported northward is relatively warm (and saline), a stronger AMOC can be assumed to also advect more heat poleward. To assess whether the positive AMOC differences of LH and HH compared to LL translate into bringing more of this warm water mass first, into the the subpolar North Atlantic and second, further into the Nordic Seas, we compute transport profiles

https://doi.org/10.5194/egusphere-2026-1481
Preprint. Discussion started: 26 May 2026

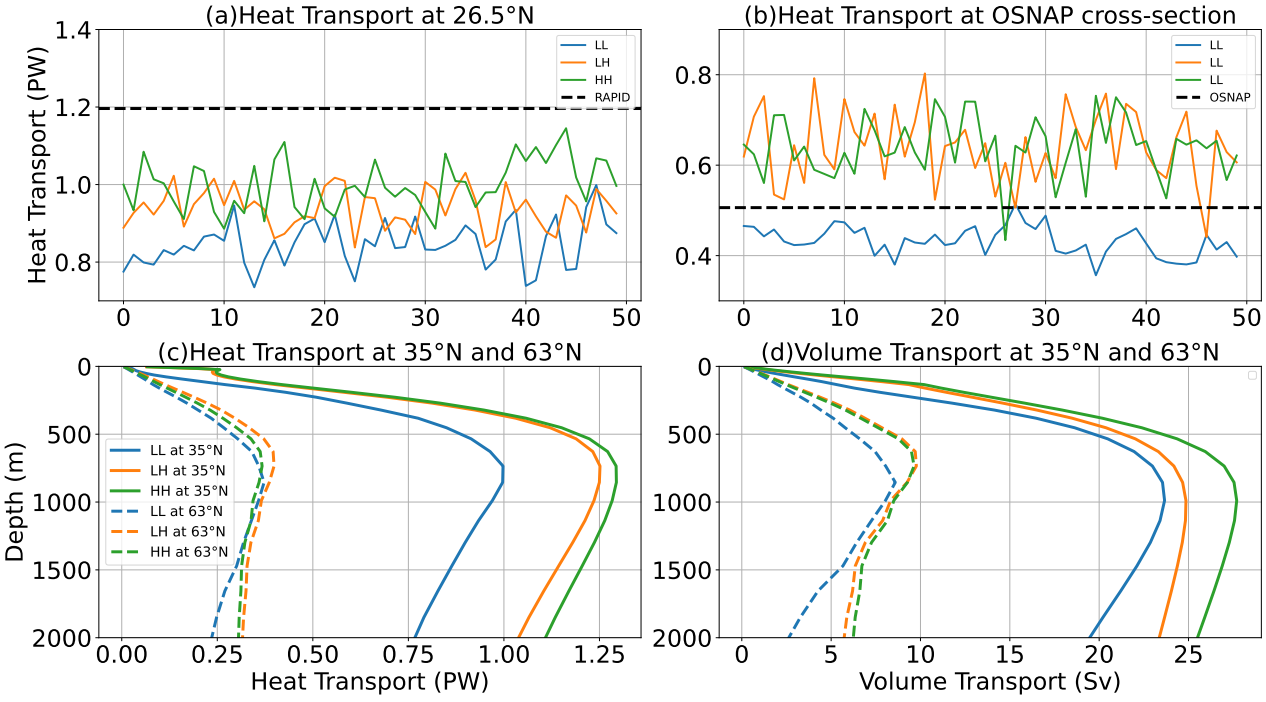

Figure 7. Time series of meridional heat transport at (a) 26.5°N and (b)OSNAP cross-section. In (a) and (b) an observational mean meridional heat ransport estimate from the RAPID and OSNAP arrays are shown as dashed black line, respectively. Time mean vertical profile of meridional (c) heat (PW) and (d) volume transport (Sv) integrated over the Gulf-Stream region (solid) and Greenland-Iceland-Scotland cross-section (dashed). The solid and/or dashed coloured line in the figures represents LL, LH, and HH model configurations.

at two cross-sections: one across the Gulf Stream just before it separates from the American shelf (∼35°N) and the other at the Greenland-Iceland-Scotland ridge (∼63°N) (Fig. 7c & d). At the 35°N cross-section, the volume transport increases with higher ocean and atmospheric model resolution where ocean resolution causes a bigger step from LL to LH but HH simulating the overall largest transport (Fig. 7d). However, at ∼63°N the volume transport of LH and HH is the same, still much larger than in LL.

The improved ocean circulation associated with the nested ocean model is clearly visible in the surface and deeper level current (Fig. 8). As the changes in ocean circulation primarily results from the high resolution ocean, we have compared LL and LH to show the changes. The LH model simulates a realistic Gulf Stream and its separation. From drifter observation, Li et al. (2022) showed the Gulf Stream separates from the US coast near Cape Hatteras at ∼35°N. In LH the Gulf Stream separates at ∼40°N whereas LL does not simulate a clear separation of the Gulf Stream (Fig. 8). The attachment of the Gulf Stream to the coast is a common issue in coarse resolution ocean model simulations (Saba et al., 2016; Schoonover et al., 2017). The LH model shows significant improvement in the pathways of the NAC which is overly zonal in the LL configuration. The better simulated NAC in LH compared to LL largely explains the reduction of the North Atlantic cold bias in LL (Fig. 2).

https://doi.org/10.5194/egusphere-2026-1481
Preprint. Discussion started: 26 May 2026

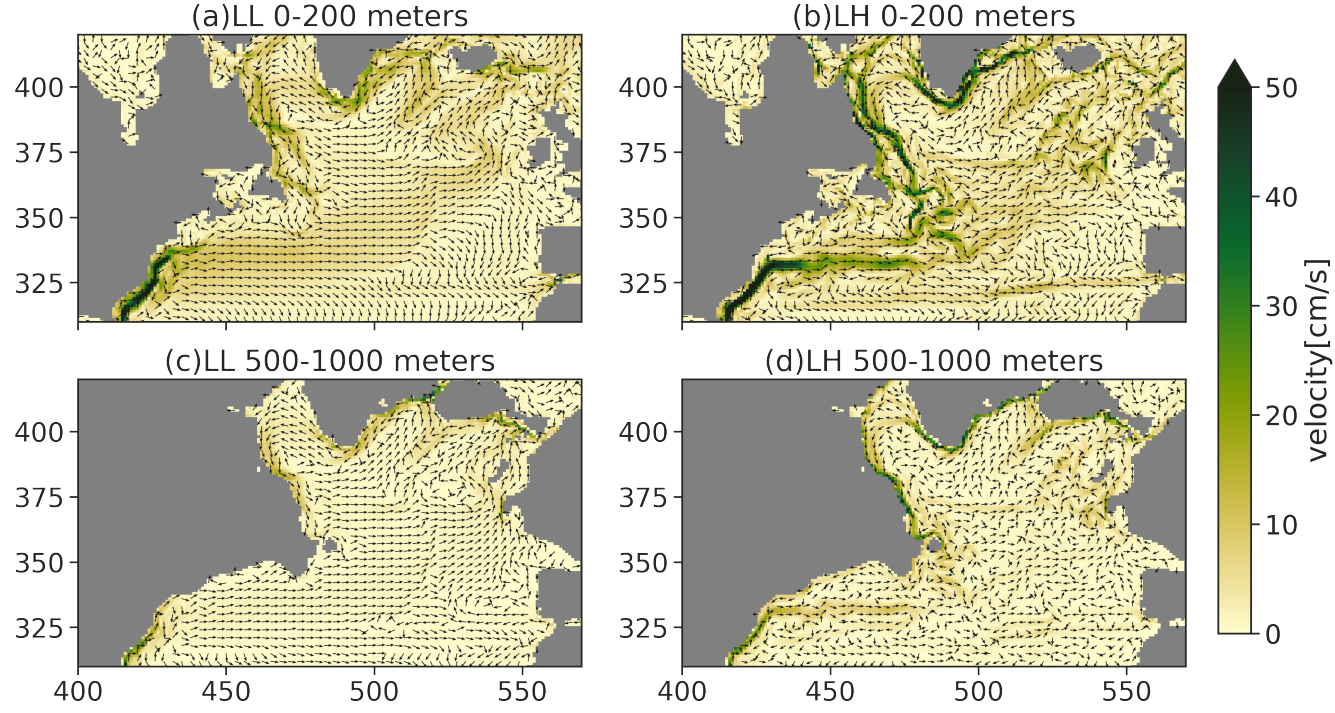

Figure 8. Annual-mean ocean current velocity (cm s^{-1}) averaged over 0–200 m (a–b) and 500-1000 m (c–d) depth. Color coding indicates current speed, arrows of standard length indicates current direction. The annual means are computed over simulations years 51–100.

With the increase in ocean resolution, ocean surface velocity fields clearly demonstrate the increase in the intensity of the main currents, such as the western boundary currents and NAC (Fig. 8).

The grid refinement also allows the LH simulations to resolve Labrador Sea eddies and intensify the Labrador Current which carries fresh and cold polar waters southward and meets the NAC at the northwest corner off Newfoundland. At this junction, mesoscale ocean dynamics influence the degree to which polar water mixes into the warm and salty waters of the NAC. The LH configuration accurately represents this interaction, while in LL, it is almost imperceptible (Fig. 8). In the strongly eddying ocean model, the Labrador Current extends southward along the coast of North America with a narrow wedge reaching the Mid-Atlantic Bight. The stronger transport of polar water through the Labrador Current causes cooling and freshening in the far west, reaching the Gulf Stream extension region (Fig. 8).

3.3 Ocean heat transport and surface heat flux

As this study focuses on transports toward the subpolar North Atlantic and the Nordic Seas, it is both relevant and necessary to evaluate the simulated meridional heat transport against observations located near the analyzed sections. To this end, we compute heat transports across the RAPID array at 26.5°N and along the OSNAP sections (Fig. 7a & b). All configurations simulate weaker heat transport at 26.5°N, with peak values of approximately 1.1 PW compared to the RAPID mean of about

https://doi.org/10.5194/egusphere-2026-1481
Preprint. Discussion started: 26 May 2026

1.2 PW (Fig. 7a). Along the OSNAP sections, however, the LH and HH configurations produce stronger transports than the observed total OSNAP estimate (Fig. 7b).

The stronger overturning circulation is, as expected, associated with an enhanced northward heat transport in the Gulf Stream (Fig. 7c). At 35°N, both the volume and heat transports exhibit a systematic increase with model resolution, from LL to LH and further to HH. The LH and HH configurations simulate a meridional heat transport of approximately 1.2–1.3 PW toward the subpolar North Atlantic, whereas the LL configuration reaches a maximum of about 1 PW. In the upper to mid-depth ocean (surface to 1000 m), the largest increase in volume transport occurs between the LH and HH configurations,(Fig. 7d), whereas the heat transport increase is largest from LL to LH (Fig. 7c). We consider the overall cooler climate in HH to be the reason for this decoupling of volume and heat incremental change.

While the heat transport at the Greenland-Iceland-Scotland section (63°N) is again lowest in LL, we find that LH conveys the largest amount of heat into the Nordic Seas despite having the same volume transport as HH (dashed lines in Fig. 7c, d). The difference in heat transport between the LH and HH configurations is approximately 0.1 PW, despite the two simulations exhibiting nearly identical volume transports. So, in HH the most heat is transported from subtropical latitudes into the subpolar North Atlantic, but less enters the polar latitudes with the Atlantic Water. Where does the heat go instead? The subpolar North Atlantic between the two cross-sections is a region of major heat loss from the ocean to the atmosphere being largest in winter but also dominating the annual mean (Fig. 9a–c). In all simulations largest heat loss is observed over the Gulf Stream extension and in the western Labrador Sea. It is this heat loss that contributes significantly to the overturning circulation by densifying the warm and saline upper ocean waters of the NAC. Remarkably, in LL larger heat loss appears to be confined to the edge of the subpolar gyre with the gyre center featuring relatively low numbers ($<$100 w/m^2). Gyre rim and interior are much less distinguishable in LH and HH and we conclude that the eddy-rich ocean contributes to widening the area of enhanced heat loss. Further, explicitly simulating mesoscale dynamics improves the position of the NAC as mentioned above, shifting the front of warm subtropical water northward into the path of the cold westerly winds, which significantly enhances heat loss in winter in LH and HH compared to LL (Fig. 9d–f). This effect is even stronger in HH than in LH. In all three model configurations, the surface fluxes are computed by the atmosphere component. Refining the ocean grid by implementing the VIKING10 nest yields not only higher SST but also a wider distribution of SST with more extreme values (Fig. 10a). However, SST is smoothed in LH when coupled to the still coarse resolution atmosphere and the information is lost for the computation of the fluxes. Nevertheless, LH simulates a wider path of the NAC than LL, which is sufficient to produce larger and thus a wider range of surface heat fluxes, here demonstrated by the dominant turbulent heat flux (Fig. 10c). With the refined atmosphere grid in HH, the wider range of SST is actually used for computing surface heat flux resulting in a greater number of occurrences of large heat fluxes ($>$170 W/m^2). The higher upward THF in HH over the SPNA compared to LH explains the higher heat convergence resulting from the differences in the meridional heat transport between HH and LH (Fig. 7c).

The winter heat loss in the SPNA via surface heat flux increases upper ocean density and also provides an important precondition for open ocean deep convection indicated by mixed layer depths exceeding 500 m and reaching a maximum in March. The LL experiment shows two distinct deep convection sites: a primary center in the Labrador Sea and a secondary center in the Irminger Sea (Fig. 9g–i). Deep mixing is also found in the Greenland Sea but to a weaker extent. Deep convection in LH

https://doi.org/10.5194/egusphere-2026-1481
Preprint. Discussion started: 26 May 2026

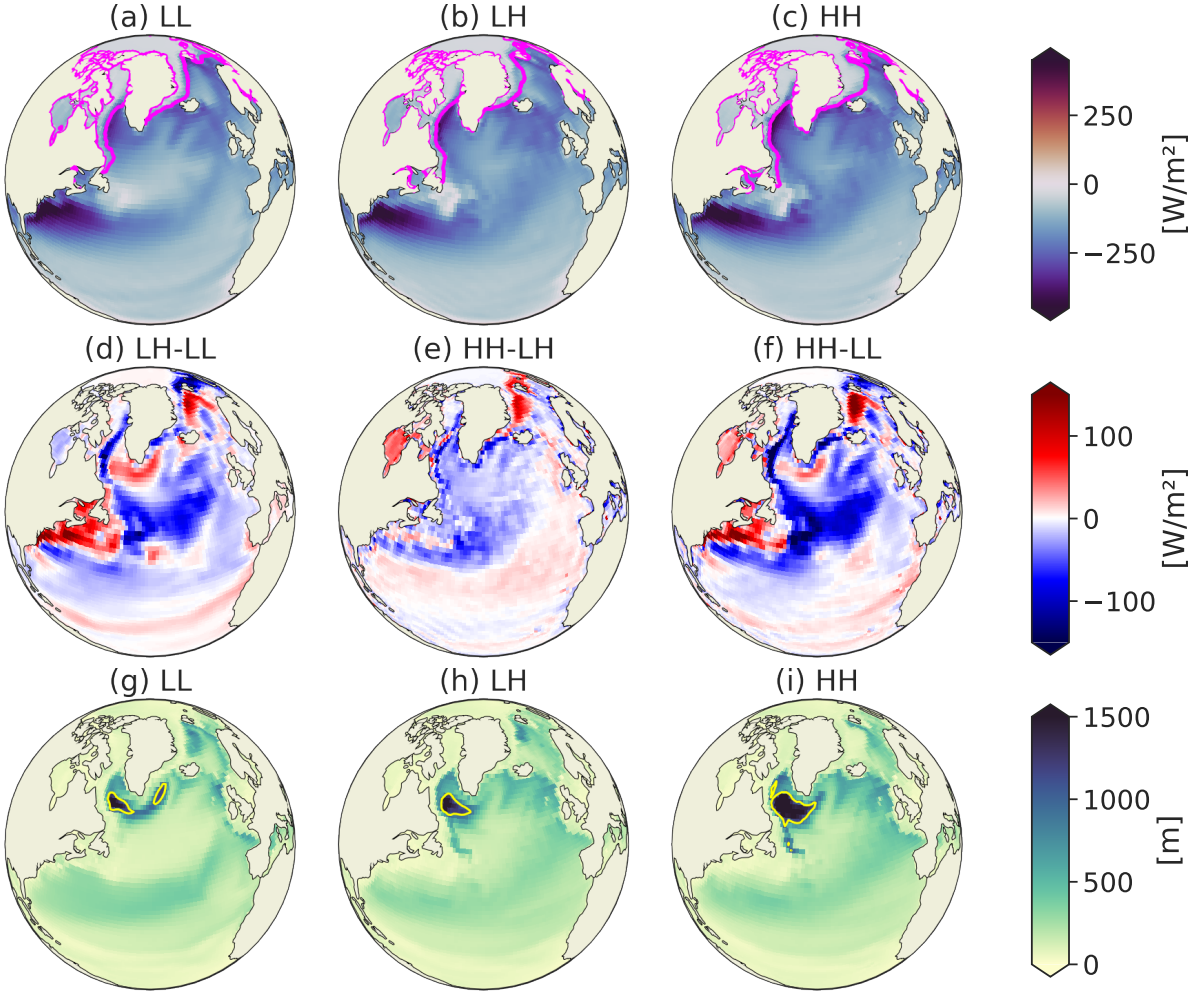

Figure 9. DJF mean surface net heat flux (a–c), difference in DJF surface net heat fluxe (d–f), March mean MLD (g–i). The magenta contours show the 15% sea-ice concentration and yellow line shows the the center of deep convection where mean MLD exceed 1000 m. The DJF means are computed over simulations years 51–100.

355 and HH is focused on the Labrador Sea. Enhanced ocean grid resolution tends to create wider areas of deep mixing there. The THF in the Irminger Sea is weaker in LH and HH compared to LL, hence both simulations with grid refinement have shallower MLD in the Irminger Sea and deep convection mainly occurs in the Labrador Sea. LH also simulates a deeper winter mixed layer in the Nordic Seas compared to LL. This is capped by a more extensive sea ice cover in HH, however, which is a feature of the overall colder climate in the latter simulation (magenta lines in Fig. 9a–c).

360 The differences in deep convection in the Greenland Sea explain the zonal mean temperature differences at 65–80°N shown in Fig. 3. Stronger deep convection cools the local ocean and warms the lower troposphere in LH−LL. A sea-ice lid and lack

https://doi.org/10.5194/egusphere-2026-1481
Preprint. Discussion started: 26 May 2026

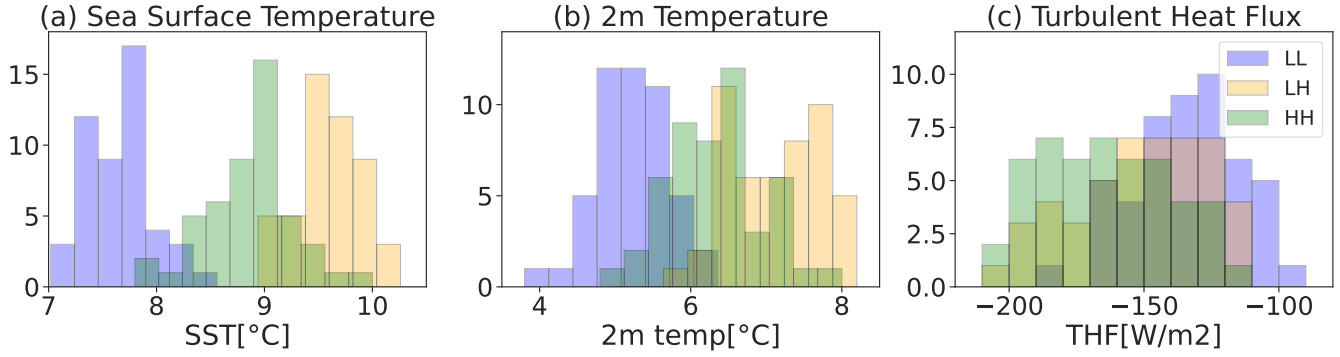

Figure 10. Histograms of the DJF mean (a) sea surface temperature, (b) 2 m air Temperature (°C), turbulent heat flux. All the variables are averaged over the sub-polar North Atlantic region (50°N–65°N and 40°W-10°W.)

of deep convection warms the mid-depth ocean and keeps the atmosphere cold in HH−LH. Interestingly, the cold response dominates in each component and thus cooling is the residual response in HH−LL.

In summary, an overview of the meridional heat transport changes from the subtropical to the subpolar regions and further poleward to the Arctic, as well as the air-sea heat flux differences are illustrated in Fig. 11. Note that we have calculated the meridional heat transport for the ocean using the global ocean. We have chosen 40°N as the boundary between subtropical and subpolar oceans to calculate the heat transport for the two regions. The oceanic heat transport from the subtropical to the subpolar North Atlantic is stronger in the LH and HH configurations than in LL, consistent with the enhanced Atlantic meridional heat transport discussed above (Fig. 7c). The associated air–sea heat fluxes exhibit contrasting behavior between the subtropical and subpolar regions. In the subpolar North Atlantic, surface heat loss to the atmosphere increases with model resolution, with the HH configuration showing the largest heat loss. In contrast, the subtropical region displays a more mixed and less systematic response across resolutions with LL having the strongest heat loss. In a coupled climate system, the meridional heat transports by the ocean and atmosphere tend to compensate for one another, a mechanism first described by Bjerknes (1964) and now referred to as Bjerknes compensation. Consistent with this framework, the enhanced oceanic meridional heat transport in the LH and HH configurations from the subtropical to the subpolar North Atlantic is accompanied by a reduction in atmospheric meridional heat transport (Fig. 11), maintaining an approximate energetic balance. However, this compensation appears to be less effective between the subpolar North Atlantic and the Arctic. In this region, the partitioning between oceanic and atmospheric heat transport is not as tightly balanced, suggesting regional differences in coupling strength and heat redistribution processes.

4 Discussion and Conclusions

This study examines the effects of oceanic and atmospheric model resolution on the mean state of the North Atlantic Ocean, with a particular focus on meridional heat transport. Our findings indicate that both oceanic and atmospheric resolutions

https://doi.org/10.5194/egusphere-2026-1481
Preprint. Discussion started: 26 May 2026

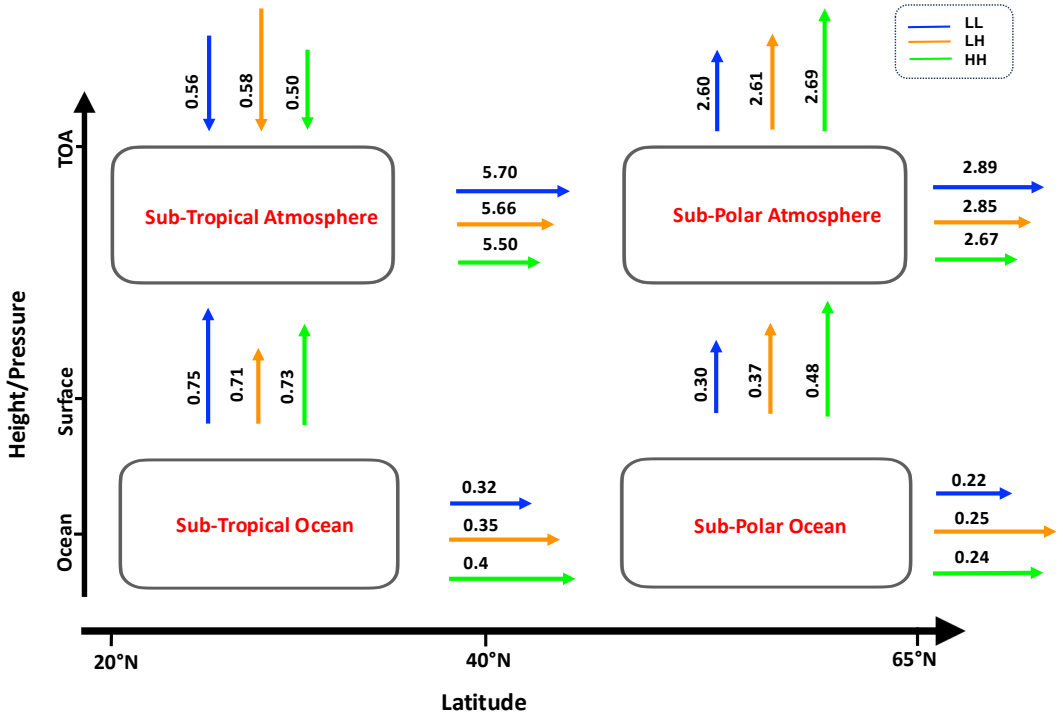

Figure 11. Sketch of meridional heat transport in PW between subtropical and subpolar latitudes in ocean and atmosphere summarizing the difference between the three model configurations.

significantly influence both surface conditions, e.g. SST and THF (Fig. 2a–c, Fig. 9d–f) as well as the deeper ocean and upper troposphere (Fig. 3). Rather than increasing the ocean horizontal resolution globally, we implemented regional grid refinement in the ocean from 1/2° to 1/10° over the North Atlantic Ocean using the 2-way AGRIF nest VIKING10 (Matthes et al., 2020; Martin and Biastoch, 2023). The grid refinement means the ocean mesh is non-eddying globally but eddy-rich between 30° and 85°N. We further increased the atmospheric resolution from ∼100 km to ∼31 km globally in a third model configuration. The three model configuration with varying oceanic and atmospheric resolution are labeled as LL, LH and HH; where LL denotes low-resolution atmosphere and non-nested ocean, LH is low-resolution atmosphere and nested ocean, and HH is high-resolution atmosphere and nested ocean. This suite of models enables us to deepen our understanding of the importance of mesoscale ocean dynamics and the need for matching atmospheric resolution for the better representation of the mean state of North Atlantic Ocean.

The annual-mean, zonal-mean temperature in the North Atlantic changes significantly with the increase in ocean resolution (Fig. 3 (a–c)), both near the surface and at depth. We observe three notable changes in temperature and salinity as model resolution increases: First, warmer and saltier waters in the upper ∼100 m over most of the North Atlantic, except for the North American east coast where there is a cooling (Fig. 4a & b). This pattern is explained by the inclusion of ocean grid refinement

https://doi.org/10.5194/egusphere-2026-1481
Preprint. Discussion started: 26 May 2026

and explicit representation of mesoscale eddy dynamics which allows the Gulf Stream and NAC to take more realistic paths in LH and HH compared to LL, similar to results by many previous studies (Marzocchi et al., 2015; Roberts et al., 2019; Delworth et al., 2012). The more realistic currents in LH and HH transport additional heat into the SPNA and bring in cold water from the Labrador current south of the Grand Banks, which reduces the cold bias in the SPNA and the warm bias on the North American shelf. The improvement in the SST bias in the nested ocean model (Fig. 2) over the North Atlantic Ocean due to improved simulation of NAC's meanders and eddies has also been reported in the FOCI model description paper (Matthes et al., 2020).

Second, colder and fresher water masses at mid-depths ($\approx$ 500–1500 m) from 0–50°N in LH and HH is observed compared to LL (Fig. 3a & c). The change at mid-depth is largely due to the reduced outflow of Mediterranean water through the Strait of Gibraltar in the LH and HH configurations, resulting from ocean grid refinement. As the ocean horizontal resolution is increased, the strait becomes narrower and shallower and there is a more realistic overflow of dense water similarly to the high-latitude overflows in Colombo et al. (2020). However, the core of the outflow water is too shallow in LH and HH (around 700 m) due to rapid mixing with Atlantic water. The limitation in the model's ability to simulate MOW and its core depth contributes to the observed mid-depth cooling in the LH and HH configurations.

Third, colder water at the surface and extending to depth along with lower air temperatures in most of the troposphere is visible in HH compared to LL and LH. The colder atmosphere and surface is caused by a lower cloud radiative forcing when using the high-resolution atmosphere in HH which in turn is due to a higher cloud erosion rate. The colder temperatures are particularly prominent in the Arctic lower troposphere, likely due to an ice-albedo feedback, as supported by a larger sea-ice cover in HH compared to LL and LH (Fig. A1).

Understanding the effect of horizontal resolution on the AMOC in coupled models is crucial, and previous studies have reported conflicting results. Our model simulations indicate that the AMOC strengthens with increased horizontal resolution (Fig. 6), which aligns with findings from some studies (Grist et al., 2018; Roberts et al., 2020, 2019; Hirschi et al., 2020), not found but disagrees with Delworth et al. (2012), who reported AMOC weakening.

The stronger AMOC in the LH and HH configuration (Fig. 6) can be attributed to several processes: 1. The finer horizontal resolution resolves Labrador Sea eddies and associated mesoscale dynamics, which are crucial to water mass transformation and densification of deep boundary currents. 2. The more substantial heat loss through THF in LH and HH than LL (Fig. 9b & c) leading to more vigorous deep convection over the Labrador Sea region and an associated increase in MLD (Fig. 9h & i). The deep water formation and deep western boundary currents may alter the sinking branch of the AMOC, leading to a strengthening of the AMOC in LH and HH. 3. Another factor contributing to the AMOC's strength is the Nordic Seas overflow, which constitutes the densest component of North Atlantic Deep Water. Colombo et al. (2020) reported that increased horizontal resolution improves the representation of the Denmark Strait overflow. We believe the stronger overflow in the nested ocean model compared to the non-nested model, significantly contributes to the strengthening of the AMOC in the LH and HH configurations.

Furthermore, we have demonstrated that the meridional heat transport associated with the AMOC increases with increasing horizontal resolution (Fig. 7c). Enhanced poleward heat transport in an eddy-resolving ocean model has been reported by

https://doi.org/10.5194/egusphere-2026-1481
Preprint. Discussion started: 26 May 2026

many studies (Roberts et al., 2018; Grist et al., 2018; Docquier et al., 2019; Hewitt et al., 2016). By performing a multi-model comparison, Grist et al. (2018) concluded that increasing both oceanic and atmospheric resolutions leads to changes in heat transport similar to those obtained by increasing ocean resolution alone. However, our results disagree with this conclusion, as we have found a significant change in heat transport when atmospheric resolution is increased (Fig. 7c). The finer horizontal resolution in the ocean model results in a notable strengthening of the major currents, such as the Gulf Stream and the North Atlantic Current, as evident from the surface velocity fields (Fig. 8). The intense warm boundary currents (Fig. 8) leads to higher SST and increased upward latent heat flux from the ocean to the atmosphere, thus providing a higher heat transport in LH and HH compared to LL (Fig. 7c).

We have estimated heat and volume transport at two crucial latitudes in the North Atlantic Ocean: the Gulf Stream region (∼35°N) and the Greenland-Iceland-Scotland (∼63°N) cross-section (Fig. 7c & d). The meridional heat transport at (∼35°N) increases with model resolution, i.e., it is lowest in LL and highest in HH (Fig. 7c). However, at (∼63°N), which marks the northern boundary of the subpolar gyre, the heat transport is stronger in LH than HH, implying heat accumulation in the subpolar gyre region (Fig. 7c). Although Roberts et al. (2020) discussed a similar increase in heat transport with enhanced ocean resolution, our study specifically highlight the differences in heat transport between the subtropical and subpolar gyre regions in a high-resolution atmospheric model. Our findings reveal that the differences in oceanic meridional heat transport between the simulations is also reflected in the atmosphere, where HH has the lowest atmospheric meridional heat transport of all simulations (Fig. 11). The increase in meridional heat transport leads to increase in mid-high-latitude SST (Fig. 4a & b) and increased latent heat loss (Fig. 9b & c) in the LH and HH configuration. The reduced Arctic sea-ice area (Fig. A1) in LH is likely driven by higher poleward heat transport and associated warming.

The deepest spring (March) MLD is primarily generated by favourable wintertime conditions, which include intense air-sea fluxes caused by dry and cold westerly winds over the Labrador and Irminger Seas, along with weak interior stratification. The nested ocean model in LH and HH, simulates a deeper mixed layer compared to the non-nested model in LL, although deep convection in the Irminger Sea is not evident in the nested models. The deepest mixed layer is simulated in HH with a high-resolution atmosphere, characterised by a deep convection region extending farther eastward. A multi-model intercomparison by (Koenigk et al., 2021) reported a similar increase in Labrador Sea deep convection with higher ocean horizontal resolution. They also found that increased atmospheric resolution has a negligible effect compared to increased ocean resolution, which does not align with our findings. However, it is essential to note that their conclusions are based on comparisons between non-eddy-permitting and eddy-permitting resolutions.

The surface heat flux (Fig. 9a–c) and its changes due to model resolution (Fig. 9d–f) effectively explain the MLD patterns. The most substantial wintertime surface heat loss in the high-resolution atmosphere configuration contributes to the deepest mixed layer. The warmer SPNA in the LH and HH configurations than in the LL configuration lead to stronger heat loss and increases deep convection in the Labrador Sea. Roberts et al. (2017) examined the SST-latent heat flux relationship in an eddy-resolving ocean model and concluded that an improved SST mean state and a sufficiently strong atmosphere-ocean coupling strength, enabling enhanced heat loss to the atmosphere, are key to reducing the heat flux bias. Improved representation of ocean-eddy–atmosphere interactions, as highlighted by Ma et al. (2016), is likely to contribute significantly as well. Our

https://doi.org/10.5194/egusphere-2026-1481
Preprint. Discussion started: 26 May 2026

findings align with this, as heat loss in the subpolar North Atlantic increases in the eddy-resolving ocean model and further enhances as we increase atmospheric resolution.

Moreover, the histograms of surface temperature and THF (Fig. 10) over the SPNA emphasize the importance of atmosphere-ocean coupling in simulating the temperature-heat flux relationship. Enhancing ocean horizontal resolution increases both surface temperature and surface heat loss in LH compared to LL. However, increasing atmospheric resolution (HH) reduces the surface temperature due to the stronger heat loss through THF compared to LH. The higher atmospheric resolution better matches the ocean resolution in HH than in LH simulating stronger coupling processes. Additionally, the enhanced heat loss from the SPNA in the HH configuration explains the heat accumulation due to meridional heat transport.

We summarise the coupled feedbacks on meridional heat transport by comparing the global atmospheric and oceanic heat transports across all three configurations (Fig. 11), thereby identifying the presence of Bjerknes compensation in maintaining the large-scale energy balance. Across the three resolutions, the compensation is more pronounced in the mid-latitudes than at high latitudes, consistent with findings by (Outten et al., 2018). They attribute this stronger mid-latitude compensation to intense air–sea interactions associated with storm track activity, where tight coupling between oceanic and atmospheric processes facilitates an efficient redistribution of heat between the two components.

The overflow of dense water through the Denmark Strait (DS) between Greenland and Iceland and the Faroe Bank Channel (FBC) between the Faroe Islands and Scotland are influenced by the heat transport from the SPNA to the Nordic Seas. We have found that heat transport to the Nordic Seas decreases with increase in atmospheric model resolution (HH). A comparison of the mean transports through the DS and FBC overflows in our model configurations shows good agreement with observational estimates. However, the LH configuration simulates noticeably stronger overflow transports in both straits compared to HH. In the DS, the transport reaches 3.6 Sv in LH, whereas HH simulates 3.3 Sv. A similar pattern is found for the FBC, where the simulated transports are 2.1 Sv in LH and 1.9 Sv in HH, respectively. The changes in the overflow transport will effectively impact the lower limb of the AMOC and, hence, could potentially feedback the strength of the AMOC. Therefore, improving the representation of processes in the SPNA and Nordic Seas, particularly deep convection and the overflow transports will enhance the representation of AMOC strength and variability.

Eiselt and Graversen (2023) reported that the CMIP models with strong AMOC have a weaker $4\times CO2$ response than models with weak AMOC, which implies, the mean AMOC state plays a significant role in setting climate sensitivity. Hence, LH and HH probably have a lower climate sensitivity due to AGRIF. However, as the simulations presented here are conducted under constant 1950 forcing conditions, we are unable to directly assess changes in climate sensitivity associated with increasing horizontal resolution. Future studies should therefore investigate the AMOC response under transient forcing scenarios. Furthermore, Roberts et al. (2020) found a stronger decline of the AMOC in high-resolution models compared to coarser-resolution counterparts in Shared Socioeconomic Pathway 8.5 (SSP5-8.5) projections. They attributed this enhanced decline to reduced dense water formation in the subpolar gyre and Labrador Sea under warming conditions. Given that our results reveal substantial resolution-dependent differences in subpolar North Atlantic processes, it will be particularly valuable to analyse future projection simulations using the three model configurations employed in this study. Such experiments would help to clarify the role of ocean resolution and regional process representation in shaping the AMOC response to climate change.

https://doi.org/10.5194/egusphere-2026-1481
Preprint. Discussion started: 26 May 2026

Code availability. FOCI-OpenIFS is composed of several component models which do not allow us to distribute the full source code due to licensing issues. OpenIFS 43r3 code was retrieved from ECMWF after signing an ECMWF license agreement and OpenIFS's licence is easily given free of charge to any academic or research institute. The details of the different versions of the OpenIFS model, including the OpenIFS version used in this study, i.e. 43r3, can be found at https://confluence.ecmwf.int/display/OIFS/About+OpenIFS (ECMWF, 2018). The full NEMO source code is available at https://doi.org/10.5281/zenodo.20306816 (Madec, 2016). The revision used in all FOCI versions is revision 6721. The configuration files (namelists etc.) for the model experiments are shared through Zenodo at https://doi.org/10.5281/zenodo.18853157. We do not have the possibility to make input and output data publicly available with a DOI. The original model simulation input and output files are stored at Kiel University and can be made available by the authors upon reasonable request. Our XIOS version is 2.5, revision 1910 from https://forge.ipsl.jussieu.fr/ioserver/svn/XIOS (Meurdesoif, 2020). OASIS is branch "OASIS3-MCT_5.0" from https://gitlab.com/cerfacs/oasis3-mct.git (Valcke et al., 2021).The observation and reanalysis datasets used in this study can be downloaded from OSNAP (https://doi.org/10.35090/gatech/70342, Fu et al., 2023), RAPID (https://rapid.ac.uk, Moat et al., 2022), and EN4 (https://www.metoffice.gov.uk/hadobs/en4/, Good et al., 2013).

Author contributions. All the model simulations were conducted by JK. SO, JK & TM conceived and refined the overall structure of the investigation based on discussions with and feedback from all co-authors. Analysis of the output and the writing of the text for this paper were coordinated by SO with substantial contributions from JK & TM. All authors have read and agreed to the current version of the manuscript.

Competing interests. The authors declare no competing interests.

Acknowledgements. We thank Sebastian Wahl for technical assistance. The model experiments were run on the NHR clusters *Emmy* and *Lise* under compute project *shk00018* and we thank the support staff for both clusters for technical support. This work was funded by the SCENIC project, an Innovation Pool initiative within the Helmholtz Program "Changing Earth - Sustaining Our Future", and also benefited from IS-ENES3 (EU Horizon 2020, grant 824084).

https://doi.org/10.5194/egusphere-2026-1481
Preprint. Discussion started: 26 May 2026

References

Athanasiadis, P. J., Ogawa, F., Omrani, N.-E., Keenlyside, N., Schiemann, R., Baker, A. J., Vidale, P. L., Bellucci, A., Ruggieri, P., Haarsma, R., Roberts, M., Roberts, C., Novak, L., and Gualdi, S.: Mitigating Climate Biases in the Midlatitude North Atlantic by Increasing Model Resolution: SST Gradients and Their Relation to Blocking and the Jet, Journal of Climate, 35, 6985 – 7006, https://doi.org/10.1175/JCLI-D-21-0515.1, 2022.

Balsamo, G., Beljaars, A., Scipal, K., Viterbo, P., van den Hurk, B., Hirschi, M., and Betts, A. K.: A Revised Hydrology for the ECMWF Model: Verification from Field Site to Terrestrial Water Storage and Impact in the Integrated Forecast System, Journal of Hydrometeorology, 10, 623 – 643, https://doi.org/10.1175/2008JHM1068.1, 2009.

Bellucci, A., Athanasiadis, P. J., Scoccimarro, E., Ruggieri, P., Gualdi, S., Fedele, G., Haarsma, R. J., Garcia-Serrano, J., Castrillo, M., Putrahasan, D., Sanchez-Gomez, E., Moine, M.-P., Roberts, C. D., Roberts, M. J., Seddon, J., and Vidale, P. L.: Air-Sea interaction over the Gulf Stream in an ensemble of HighResMIP present climate simulations, Climate Dynamics, 56, 2093–2111, https://doi.org/10.1007/s00382-020-05573-z, 2021.

Biastoch, A., Böning, C. W., and Lutjeharms, J. R. E.: Agulhas leakage dynamics affects decadal variability in Atlantic overturning circulation, Nature, 456, 489–492, https://doi.org/10.1038/nature07426, 2008a.

Biastoch, A., Böning, C. W., Getzlaff, J., Molines, J.-M., and Madec, G.: Causes of Interannual–Decadal Variability in the Meridional Overturning Circulation of the Midlatitude North Atlantic Ocean, Journal of Climate, 21, 6599 – 6615, https://doi.org/10.1175/2008JCLI2404.1, 2008b.

Biastoch, A., Sein, D., Durgadoo, J. V., Wang, Q., and Danilov, S.: Simulating the Agulhas system in global ocean models – nesting vs. multi-resolution unstructured meshes, Ocean Modelling, 121, 117–131, https://doi.org/https://doi.org/10.1016/j.ocemod.2017.12.002, 2018.

Bryan, F. O., Hecht, M. W., and Smith, R. D.: Resolution convergence and sensitivity studies with North Atlantic circulation models. Part I: The western boundary current system, Ocean Modelling, 16, 141–159, https://doi.org/https://doi.org/10.1016/j.ocemod.2006.08.005, 2007.

Colombo, P., Barnier, B., Penduff, T., Chanut, J., Deshayes, J., Molines, J.-M., Le Sommer, J., Verezemskaya, P., Gulev, S., and Treguier, A.-M.: Representation of the Denmark Strait overflow in a z-coordinate eddying configuration of the NEMO (v3.6) ocean model: resolution and parameter impacts, Geoscientific Model Development, 13, 3347–3371, https://doi.org/10.5194/gmd-13-3347-2020, 2020.

Craig, A., Valcke, S., and Coquart, L.: Development and performance of a new version of the OASIS coupler, OASIS3-MCT_3.0, Geoscientific Model Development, 10, 3297–3308, https://doi.org/10.5194/gmd-10-3297-2017, 2017.

Debreu, L. and Blayo, E.: Two-way embedding algorithms: A review : Sbmitted to Ocean Dynamics: Special Issue on Multi-Scale Modelling: Nested Grid and Unstructured Mesh Approaches, Ocean Dynamics, 58, 415–428, https://doi.org/10.1007/s10236-008-0150-9, 2008.

Delworth, T. L., Rosati, A., Anderson, W., Adcroft, A. J., Balaji, V., Benson, R., Dixon, K., Griffies, S. M., Lee, H.-C., Pacanowski, R. C., Vecchi, G. A., Wittenberg, A. T., Zeng, F., and Zhang, R.: Simulated Climate and Climate Change in the GFDL CM2.5 High-Resolution Coupled Climate Model, Journal of Climate, 25, 2755 – 2781, https://doi.org/10.1175/JCLI-D-11-00316.1, 2012.

Docquier, D., Grist, J. P., Roberts, M. J., Roberts, C. D., Semmler, T., Ponsoni, L., Massonnet, F., Sidorenko, D., Sein, D. V., Iovino, D., Bellucci, A., and Fichefet, T.: Impact of model resolution on Arctic sea ice and North Atlantic Ocean heat transport, Climate Dynamics, 53, 4989–5017, https://doi.org/10.1007/s00382-019-04840-y, 2019.

ECMWF: OpenIFS programme, https://confluence.ecmwf.int/display/OIFS/About+OpenIFS, eCMWF [software], last access: 28 February 2024, 2018.

https://doi.org/10.5194/egusphere-2026-1481
Preprint. Discussion started: 26 May 2026

Eiselt, K.-U. and Graversen, R. G.: On the Control of Northern Hemispheric Feedbacks by AMOC: Evidence from CMIP and Slab Ocean Modeling, Journal of Climate, 36, 6777 – 6795, https://doi.org/10.1175/JCLI-D-22-0884.1, 2023.

Fichefet, T. and Maqueda, M. A. M.: Sensitivity of a global sea ice model to the treatment of ice thermodynamics and dynamics, Journal of Geophysical Research: Oceans, 102, 12 609–12 646, https://doi.org/https://doi.org/10.1029/97JC00480, 1997.

Fu, Y., Lozier, M. S., Biló, T. C., Bower, A. S., Cunningham, S. A., Cyr, F., de Jong, M. F., deYoung, B., Drysdale, L., Fraser, N., Fried, N., Furey, H. H., Han, G., Handmann, P., Holliday, N. P., Holte, J., Inall, M. E., Johns, W. E., Jones, S., Karstensen, J., Li, F., Pacini, A., Pickart, R. S., Rayner, D., Straneo, F., and Yashayaev, I.: Meridional Overturning Circulation Observed by the Overturning in the Subpolar North Atlantic Program (OSNAP) Array from August 2014 to June 2020, https://doi.org/10.35090/gatech/70342, 2023.

Ganachaud, A. and Wunsch, C.: Improved estimates of global ocean circulation, heat transport and mixing from hydrographic data, Nature, 408, 453–457, https://doi.org/10.1038/35044048, 2000.

Gent, P. R. and Mcwilliams, J. C.: Isopycnal Mixing in Ocean Circulation Models, Journal of Physical Oceanography, 20, 150 – 155, https://doi.org/10.1175/1520-0485(1990)020<0150:IMIOCM>2.0.CO;2, 1990.

Good, S. A., Martin, M. J., and Rayner, N. A.: EN4: Quality controlled ocean temperature and salinity profiles and monthly objective analyses with uncertainty estimates, Journal of Geophysical Research: Oceans, 118, 6704–6716, https://doi.org/https://doi.org/10.1002/2013JC009067, 2013.

Griffies, S. M., Winton, M., Anderson, W. G., Benson, R., Delworth, T. L., Dufour, C. O., Dunne, J. P., Goddard, P., Morrison, A. K., Rosati, A., Wittenberg, A. T., Yin, J., and Zhang, R.: Impacts on Ocean Heat from Transient Mesoscale Eddies in a Hierarchy of Climate Models, Journal of Climate, 28, 952 – 977, https://doi.org/10.1175/JCLI-D-14-00353.1, 2015.

Grist, J. P., Josey, S. A., New, A. L., Roberts, M., Koenigk, T., and Iovino, D.: Increasing Atlantic Ocean Heat Transport in the Latest Generation Coupled Ocean-Atmosphere Models: The Role of Air-Sea Interaction, Journal of Geophysical Research: Oceans, 123, 8624–8637, https://doi.org/https://doi.org/10.1029/2018JC014387, 2018.

Hall, M. M. and Bryden, H. L.: Direct estimates and mechanisms of ocean heat transport, Deep Sea Research Part A. Oceanographic Research Papers, 29, 339–359, https://doi.org/https://doi.org/10.1016/0198-0149(82)90099-1, 1982.

Hazeleger, W. and Bintanja, R.: Studies with the EC-Earth seamless earth system prediction model, Climate Dynamics, 39, 2609–2610, https://doi.org/10.1007/s00382-012-1577-8, 2012.

Hewitt, H. T., Roberts, M. J., Hyder, P., Graham, T., Rae, J., Belcher, S. E., Bourdallé-Badie, R., Copsey, D., Coward, A., Guiavarch, C., Harris, C., Hill, R., Hirschi, J. J.-M., Madec, G., Mizielinski, M. S., Neininger, E., New, A. L., Rioual, J.-C., Sinha, B., Storkey, D., Shelly, A., Thorpe, L., and Wood, R. A.: The impact of resolving the Rossby radius at mid-latitudes in the ocean: results from a high-resolution version of the Met Office GC2 coupled model, Geoscientific Model Development, 9, 3655–3670, https://doi.org/10.5194/gmd-9-3655-2016, 2016.

Hirschi, J. J.-M., Barnier, B., Böning, C., Biastoch, A., Blaker, A. T., Coward, A., Danilov, S., Drijfhout, S., Getzlaff, K., Griffies, S. M., Hasumi, H., Hewitt, H., Iovino, D., Kawasaki, T., Kiss, A. E., Koldunov, N., Marzocchi, A., Mecking, J. V., Moat, B., Molines, J.-M., Myers, P. G., Penduff, T., Roberts, M., Treguier, A.-M., Sein, D. V., Sidorenko, D., Small, J., Spence, P., Thompson, L., Weijer, W., and Xu, X.: The Atlantic Meridional Overturning Circulation in High-Resolution Models, Journal of Geophysical Research: Oceans, 125, e2019JC015 522, https://doi.org/https://doi.org/10.1029/2019JC015522, e2019JC015522 2019JC015522, 2020.

Hobbs, W. R. and Willis, J. K.: Midlatitude North Atlantic heat transport: A time series based on satellite and drifter data, Journal of Geophysical Research: Oceans, 117, https://doi.org/https://doi.org/10.1029/2011JC007039, 2012.

https://doi.org/10.5194/egusphere-2026-1481
Preprint. Discussion started: 26 May 2026

Hortal, M.: The development and testing of a new two-time-level semi-Lagrangian scheme (SETTLS) in the ECMWF forecast model, Quarterly Journal of the Royal Meteorological Society, 128, 1671–1687, https://doi.org/https://doi.org/10.1002/qj.200212858314, 2002.

Hsiung, J.: Estimates of Global Oceanic Meridional Heat Transport, Journal of Physical Oceanography, 15, 1405 – 1413, https://doi.org/10.1175/1520-0485(1985)015<1405:EOGOMH>2.0.CO;2, 1985.

Johns, W. E., Baringer, M. O., Beal, L. M., Cunningham, S. A., Kanzow, T., Bryden, H. L., Hirschi, J. J. M., Marotzke, J., Meinen, C. S., Shaw, B., and Curry, R.: Continuous, Array-Based Estimates of Atlantic Ocean Heat Transport at 26.5°N, Journal of Climate, 24, 2429 – 2449, https://doi.org/10.1175/2010JCLI3997.1, 2011.

Kjellsson, J. and Zanna, L.: The Impact of Horizontal Resolution on Energy Transfers in Global Ocean Models, Fluids, 2, 45, https://doi.org/10.3390/fluids2030045, 2017.

Kjellsson, J., Streffing, J., Carver, G., and Köhler, M.: From weather forecasting to climate modelling using OpenIFS, ECMWF Newsletter, pp. 38–, https://doi.org/10.21957/469hc10jk5, 2020.

Koenigk, T., Fuentes-Franco, R., Meccia, V. L., Gutjahr, O., Jackson, L. C., New, A. L., Ortega, P., Roberts, C. D., Roberts, M. J., Arsouze, T., Iovino, D., Moine, M.-P., and Sein, D. V.: Deep mixed ocean volume in the Labrador Sea in HighResMIP models, Climate Dynamics, 57, 1895–1918, https://doi.org/10.1007/s00382-021-05785-x, 2021.

Koltermann, K., Sokov, A., Tereschenkov, V., Dobroliubov, S., Lorbacher, K., and Sy, A.: Decadal changes in the thermohaline circulation of the North Atlantic, Deep Sea Research Part II: Topical Studies in Oceanography, 46, 109–138, https://doi.org/https://doi.org/10.1016/S0967-0645(98)00115-5, 1999.

Kuhlbrodt, T., Jones, C. G., Sellar, A., Storkey, D., Blockley, E., Stringer, M., Hill, R., Graham, T., Ridley, J., Blaker, A., Calvert, D., Copsey, D., Ellis, R., Hewitt, H., Hyder, P., Ineson, S., Mulcahy, J., Siahaan, A., and Walton, J.: The Low-Resolution Version of HadGEM3 GC3.1: Development and Evaluation for Global Climate, Journal of Advances in Modeling Earth Systems, 10, 2865–2888, https://doi.org/https://doi.org/10.1029/2018MS001370, 2018.

Legg, S., Briegleb, B., Chang, Y., Chassignet, E. P., Danabasoglu, G., Ezer, T., Gordon, A. L., Griffies, S., Hallberg, R., Jackson, L., Large, W., Özgökmen, T. M., Peters, H., Price, J., Riemenschneider, U., Wu, W., Xu, X., and Yang, J.: Improving Oceanic Overflow Representation in Climate Models: The Gravity Current Entrainment Climate Process Team, Bulletin of the American Meteorological Society, 90, 657 – 670, https://doi.org/10.1175/2008BAMS2667.1, 2009.

Li, D., Chang, P., Yeager, S. G., Danabasoglu, G., Castruccio, F. S., Small, J., Wang, H., Zhang, Q., and Gopal, A.: The Impact of Horizontal Resolution on Projected Sea-Level Rise Along US East Continental Shelf With the Community Earth System Model, Journal of Advances in Modeling Earth Systems, 14, e2021MS002 868, https://doi.org/https://doi.org/10.1029/2021MS002868, e2021MS002868 2021MS002868, 2022.

Lozier, M. S., Li, F., Bacon, S., Bahr, F., Bower, A. S., Cunningham, S. A., de Jong, M. F., de Steur, L., deYoung, B., Fischer, J., Gary, S. F., Greenan, B. J. W., Holliday, N. P., Houk, A., Houpert, L., Inall, M. E., Johns, W. E., Johnson, H. L., Johnson, C., Karstensen, J., Koman, G., Bras, I. A. L., Lin, X., Mackay, N., Marshall, D. P., Mercier, H., Oltmanns, M., Pickart, R. S., Ramsey, A. L., Rayner, D., Straneo, F., Thierry, V., Torres, D. J., Williams, R. G., Wilson, C., Yang, J., Yashayaev, I., and Zhao, J.: A sea change in our view of overturning in the subpolar North Atlantic, Science, 363, 516–521, https://doi.org/10.1126/science.aau6592, 2019.

Ma, X., Jing, Z., Chang, P., Liu, X., Montuoro, R., Small, R. J., Bryan, F. O., Greatbatch, R. J., Brandt, P., Wu, D., Lin, X., and Wu, L.: Western boundary currents regulated by interaction between ocean eddies and the atmosphere, Nature, 535, 533–537, https://doi.org/10.1038/nature18640, 2016.

Madec, G.: NEMO ocean engine, Note du Pôle Modélisation 27, Institut Pierre-Simon Laplace (IPSL), ISSN 1288-1619, 2016.

https://doi.org/10.5194/egusphere-2026-1481
Preprint. Discussion started: 26 May 2026

Maisonnave, E.: OASIS Dedicated Support – 4th Annual Summary, Technical Report TR/CMGC/19/149, CECI, UMR CERFACS/CNRS No. 5318, France, 2019.

Maisonnave, E.: How to Interpolate Atmosphere Fluxes to an AGRIF Zoom? The ECHAM & OpenIFS Test Case (in French), Technical Report TR/CMGC/21/200, CECI, UMR CERFACS/CNRS No. 5318, France, 2021.

Martin, T. and Biastoch, A.: On the ocean's response to enhanced Greenland runoff in model experiments: relevance of mesoscale dynamics and atmospheric coupling, Ocean Science, 19, 141–167, https://doi.org/10.5194/os-19-141-2023, 2023.

Marzocchi, A., Hirschi, J. J.-M., Holliday, N. P., Cunningham, S. A., Blaker, A. T., and Coward, A. C.: The North Atlantic subpolar circulation in an eddy-resolving global ocean model, Journal of Marine Systems, 142, 126–143, https://doi.org/https://doi.org/10.1016/j.jmarsys.2014.10.007, 2015.

Matthes, K., Biastoch, A., Wahl, S., Harlaß, J., Martin, T., Brücher, T., Drews, A., Ehlert, D., Getzlaff, K., Krüger, F., Rath, W., Scheinert, M., Schwarzkopf, F. U., Bayr, T., Schmidt, H., and Park, W.: The Flexible Ocean and Climate Infrastructure version 1 (FOCI1): mean state and variability, Geoscientific Model Development, 13, 2533–2568, https://doi.org/10.5194/gmd-13-2533-2020, 2020.

Meccia, V. L., Fuentes-Franco, R., Davini, P., Bellomo, K., Fabiano, F., Yang, S., and von Hardenberg, J.: Internal multi-centennial variability of the Atlantic Meridional Overturning Circulation simulated by EC-Earth3, Climate Dynamics, 60, 3695–3712, https://doi.org/10.1007/s00382-022-06534-4, 2023.

Menary, M. B., Kuhlbrodt, T., Ridley, J., Andrews, M. B., Dimdore-Miles, O. B., Deshayes, J., Eade, R., Gray, L., Ineson, S., Mignot, J., Roberts, C. D., Robson, J., Wood, R. A., and Xavier, P.: Preindustrial Control Simulations With HadGEM3-GC3.1 for CMIP6, Journal of Advances in Modeling Earth Systems, 10, 3049–3075, https://doi.org/https://doi.org/10.1029/2018MS001495, 2018.

Meurdesoif, Y.: XIOS: Current Developments and Roadmap, https://forge.ipsl.jussieu.fr/ioserver, presentation / technical report, 2020.

Minobe, S., Kuwano-Yoshida, A., Komori, N., Xie, S.-P., and Small, R. J.: Influence of the Gulf Stream on the troposphere, Nature, 452, 206–209, https://doi.org/10.1038/nature06690, 2008.

Moat, B. I., Frajka-Williams, E., Smeed, D. A., Rayner, D., Johns, W. E., Baringer, M. O., Volkov, D., and Collins, J.: Atlantic Meridional Overturning Circulation observed by the RAPID-MOCHA-WBTS array at 26°N from 2004 to 2020 (v2020.2), https://doi.org/10.5285/e91b10af-6f0a-7fa7-e053-6c86abc05a09, 2022.

Omrani, N.-E., Ogawa, F., Nakamura, H., Keenlyside, N., Lubis, S. W., and Matthes, K.: Key Role of the Ocean Western Boundary currents in shaping the Northern Hemisphere climate, Scientific Reports, 9, 3014, https://doi.org/10.1038/s41598-019-39392-y, 2019.

Outten, S., Esau, I., and Otterå, O. H.: Bjerknes Compensation in the CMIP5 Climate Models, Journal of Climate, 31, 8745 – 8760, https://doi.org/10.1175/JCLI-D-18-0058.1, 2018.

Rackow, T., Goessling, H. F., Jung, T., Sidorenko, D., Semmler, T., Barbi, D., and Handorf, D.: Towards multi-resolution global climate modeling with ECHAM6-FESOM. Part II: climate variability, Climate Dynamics, 50, 2369–2394, https://doi.org/10.1007/s00382-016-3192-6, 2018.

Renault, L., Molemaker, M. J., Gula, J., Masson, S., and McWilliams, J. C.: Control and Stabilization of the Gulf Stream by Oceanic Current Interaction with the Atmosphere, Journal of Physical Oceanography, 46, 3439 – 3453, https://doi.org/10.1175/JPO-D-16-0115.1, 2016.

Ringler, T., Petersen, M., Higdon, R. L., Jacobsen, D., Jones, P. W., and Maltrud, M.: A multi-resolution approach to global ocean modeling, Ocean Modelling, 69, 211–232, https://doi.org/https://doi.org/10.1016/j.ocemod.2013.04.010, 2013.

Roberts, C. D., Palmer, M. D., Allan, R. P., Desbruyeres, D., Hyder, P., Liu, C., and Smith, D.: Surface flux and ocean heat transport convergence contributions to seasonal and interannual variations of ocean heat content, Journal of Geophysical Research: Oceans, 122, 726–744, https://doi.org/https://doi.org/10.1002/2016JC012278, 2017.

https://doi.org/10.5194/egusphere-2026-1481
Preprint. Discussion started: 26 May 2026

Roberts, C. D., Senan, R., Molteni, F., Boussetta, S., Mayer, M., and Keeley, S. P. E.: Climate model configurations of the ECMWF Integrated Forecasting System (ECMWF-IFS cycle 43r1) for HighResMIP, Geoscientific Model Development, 11, 3681–3712, https://doi.org/10.5194/gmd-11-3681-2018, 2018.

Roberts, M. J., Baker, A., Blockley, E. W., Calvert, D., Coward, A., Hewitt, H. T., Jackson, L. C., Kuhlbrodt, T., Mathiot, P., Roberts, C. D., Schiemann, R., Seddon, J., Vannière, B., and Vidale, P. L.: Description of the resolution hierarchy of the global coupled HadGEM3-GC3.1 model as used in CMIP6 HighResMIP experiments, Geoscientific Model Development, 12, 4999–5028, https://doi.org/10.5194/gmd-12-4999-2019, publisher: Copernicus GmbH, 2019.

Roberts, M. J., Jackson, L. C., Roberts, C. D., Meccia, V., Docquier, D., Koenigk, T., Ortega, P., Moreno-Chamarro, E., Bellucci, A., Coward, A., Drijfhout, S., Exarchou, E., Gutjahr, O., Hewitt, H., Iovino, D., Lohmann, K., Putrasahan, D., Schiemann, R., Seddon, J., Terray, L., Xu, X., Zhang, Q., Chang, P., Yeager, S. G., Castruccio, F. S., Zhang, S., and Wu, L.: Sensitivity of the Atlantic Meridional Overturning Circulation to Model Resolution in CMIP6 HighResMIP Simulations and Implications for Future Changes, Journal of Advances in Modeling Earth Systems, 12, e2019MS002 014, https://doi.org/https://doi.org/10.1029/2019MS002014, e2019MS002014 2019MS002014, 2020.

Saba, V. S., Griffies, S. M., Anderson, W. G., Winton, M., Alexander, M. A., Delworth, T. L., Hare, J. A., Harrison, M. J., Rosati, A., Vecchi, G. A., and Zhang, R.: Enhanced warming of the Northwest Atlantic Ocean under climate change, Journal of Geophysical Research: Oceans, 121, 118–132, https://doi.org/https://doi.org/10.1002/2015JC011346, 2016.

Savita, A., Kjellsson, J., Pilch Kedzierski, R., Latif, M., Rahm, T., Wahl, S., and Park, W.: Assessment of climate biases in OpenIFS version 43r3 across model horizontal resolutions and time steps, Geoscientific Model Development, 17, 1813–1829, https://doi.org/10.5194/gmd-17-1813-2024, 2024.

Schoonover, J., Dewar, W. K., Wienders, N., and Deremble, B.: Local Sensitivities of the Gulf Stream Separation, Journal of Physical Oceanography, 47, 353 – 373, https://doi.org/10.1175/JPO-D-16-0195.1, 2017.

Schwarzkopf, F. U., Biastoch, A., Böning, C. W., Chanut, J., Durgadoo, J. V., Getzlaff, K., Harlaß, J., Rieck, J. K., Roth, C., Scheinert, M. M., and Schubert, R.: The INALT family – a set of high-resolution nests for the Agulhas Current system within global NEMO ocean/sea-ice configurations, Geoscientific Model Development, 12, 3329–3355, https://doi.org/10.5194/gmd-12-3329-2019, 2019.

Sidorenko, D., Rackow, T., Jung, T., Semmler, T., Barbi, D., Danilov, S., Dethloff, K., Dorn, W., Fieg, K., Goessling, H. F., Handorf, D., Harig, S., Hiller, W., Juricke, S., Losch, M., Schröter, J., Sein, D. V., and Wang, Q.: Towards multi-resolution global climate modeling with ECHAM6–FESOM. Part I: model formulation and mean climate, Climate Dynamics, 44, 757–780, https://doi.org/10.1007/s00382-014-2290-6, 2015.

Sieker, T., Kjellsson, J., and Park, W.: Impact of ocean resolution on the North Atlantic bias in the FOCI-OpenIFS climate model. (In Press / Accepted), Climate Dynamics, https://doi.org/10.1007/s00382-026-08110-6., 2026.

Small, R. J., Tomas, R. A., and Bryan, F. O.: Storm track response to ocean fronts in a global high-resolution climate model, Climate Dynamics, 43, 805–828, https://doi.org/10.1007/s00382-013-1980-9, 2014.

Stevens, B., Giorgetta, M., Esch, M., Mauritsen, T., Crueger, T., Rast, S., Salzmann, M., Schmidt, H., Bader, J., Block, K., Brokopf, R., Fast, I., Kinne, S., Kornblueh, L., Lohmann, U., Pincus, R., Reichler, T., and Roeckner, E.: Atmospheric component of the MPI-M Earth System Model: ECHAM6, Journal of Advances in Modeling Earth Systems, 5, 146–172, https://doi.org/https://doi.org/10.1002/jame.20015, 2013.

Sérazin, G., Penduff, T., Grégorio, S., Barnier, B., Molines, J.-M., and Terray, L.: Intrinsic Variability of Sea Level from Global Ocean Simulations: Spatiotemporal Scales, Journal of Climate, 28, 4279 – 4292, https://doi.org/10.1175/JCLI-D-14-00554.1, 2015.

Talley, L. D.: Shallow, Intermediate, and Deep Overturning Components of the Global Heat Budget, Journal of Physical Oceanography, 33, 530 – 560, https://doi.org/10.1175/1520-0485(2003)033<0530:SIADOC>2.0.CO;2, 2003.

https://doi.org/10.5194/egusphere-2026-1481
Preprint. Discussion started: 26 May 2026

Temperton, C., Hortal, M., and Simmons, A.: A two-time-level semi-Lagrangian global spectral model, Quarterly Journal of the Royal Meteorological Society, 127, 111–127, https://doi.org/https://doi.org/10.1002/qj.49712757107, 2001.

Treguier, A. M., Held, I. M., and Larichev, V. D.: Parameterization of Quasigeostrophic Eddies in Primitive Equation Ocean Models, Journal of Physical Oceanography, 27, 567 – 580, https://doi.org/10.1175/1520-0485(1997)027<0567:POQEIP>2.0.CO;2, 1997.

Trenberth, K. E. and Caron, J. M.: Estimates of Meridional Atmosphere and Ocean Heat Transports, Journal of Climate, 14, 3433 – 3443, https://doi.org/10.1175/1520-0442(2001)014<3433:EOMAAO>2.0.CO;2, 2001.

Trenberth, K. E. and Fasullo, J. T.: Atlantic meridional heat transports computed from balancing Earth's energy locally, Geophysical Research Letters, 44, 1919–1927, https://doi.org/https://doi.org/10.1002/2016GL072475, 2017.

Valcke, S., Craig, A., Maisonnave, E., and Coquart, L.: OASIS3-MCT User Guide, Version 5.0, Tech. Rep. TR/CMGC/21/38, CERFACS, Toulouse, France, https://www.cerfacs.fr/oa4web/oasis3-mct_5.0/oasis3mct_UserGuide.pdf, 2021.

Wang, Q., Danilov, S., and Schröter, J.: Finite element ocean circulation model based on triangular prismatic elements, with application in studying the effect of topography representation, Journal of Geophysical Research: Oceans, 113, https://doi.org/https://doi.org/10.1029/2007JC004482, 2008.

Wuebbles, D., Meehl, G., Hayhoe, K., Karl, T. R., Kunkel, K., Santer, B., Wehner, M., Colle, B., Fischer, E. M., Fu, R., Goodman, A., Janssen, E., Kharin, V., Lee, H., Li, W., Long, L. N., Olsen, S. C., Pan, Z., Seth, A., Sheffield, J., and Sun, L.: CMIP5 Climate Model Analyses: Climate Extremes in the United States, Bulletin of the American Meteorological Society, 95, 571 – 583, https://doi.org/10.1175/BAMS-D-12-00172.1, 2014.

Zhai, X., Johnson, H. L., and Marshall, D. P.: Significant sink of ocean-eddy energy near western boundaries, Nature Geoscience, 3, 608–612, https://doi.org/10.1038/ngeo943, 2010.

https://doi.org/10.5194/egusphere-2026-1481
Preprint. Discussion started: 26 May 2026

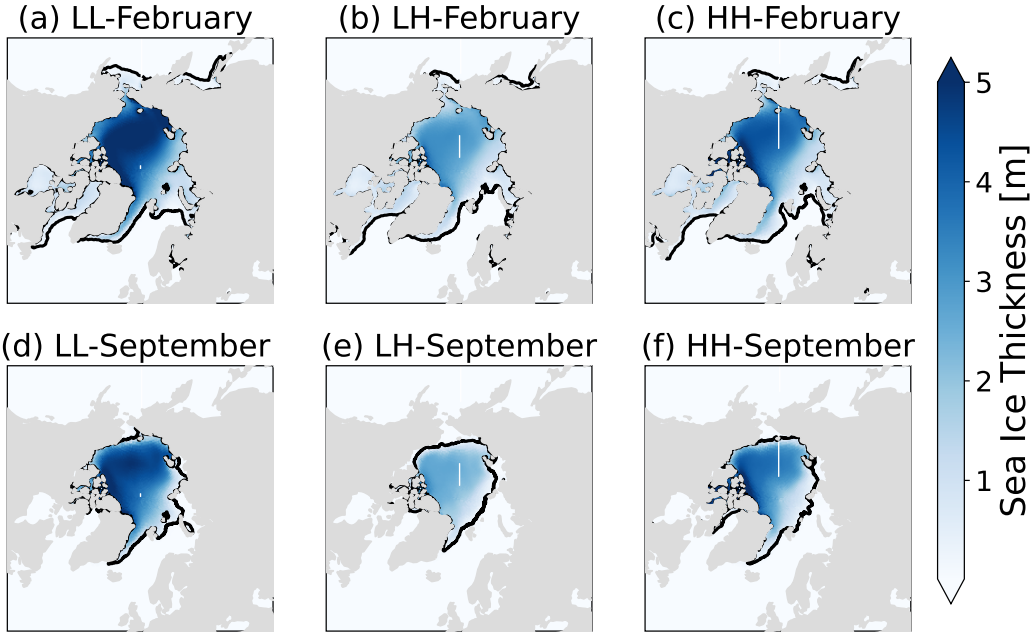

Figure A1. Annual mean sea-ice thickness, ice-edge position are shown over simulations years 51–100. The ice edge is defined by the 15% sea-ice concentration contour shown as a magenta outline. March (a–c) and September(d–f) means represent winter maximum and summer minimum spatial distributions for the Arctic. The annual means are computed over simulations years 51–100.

https://doi.org/10.5194/egusphere-2026-1481
Preprint. Discussion started: 26 May 2026

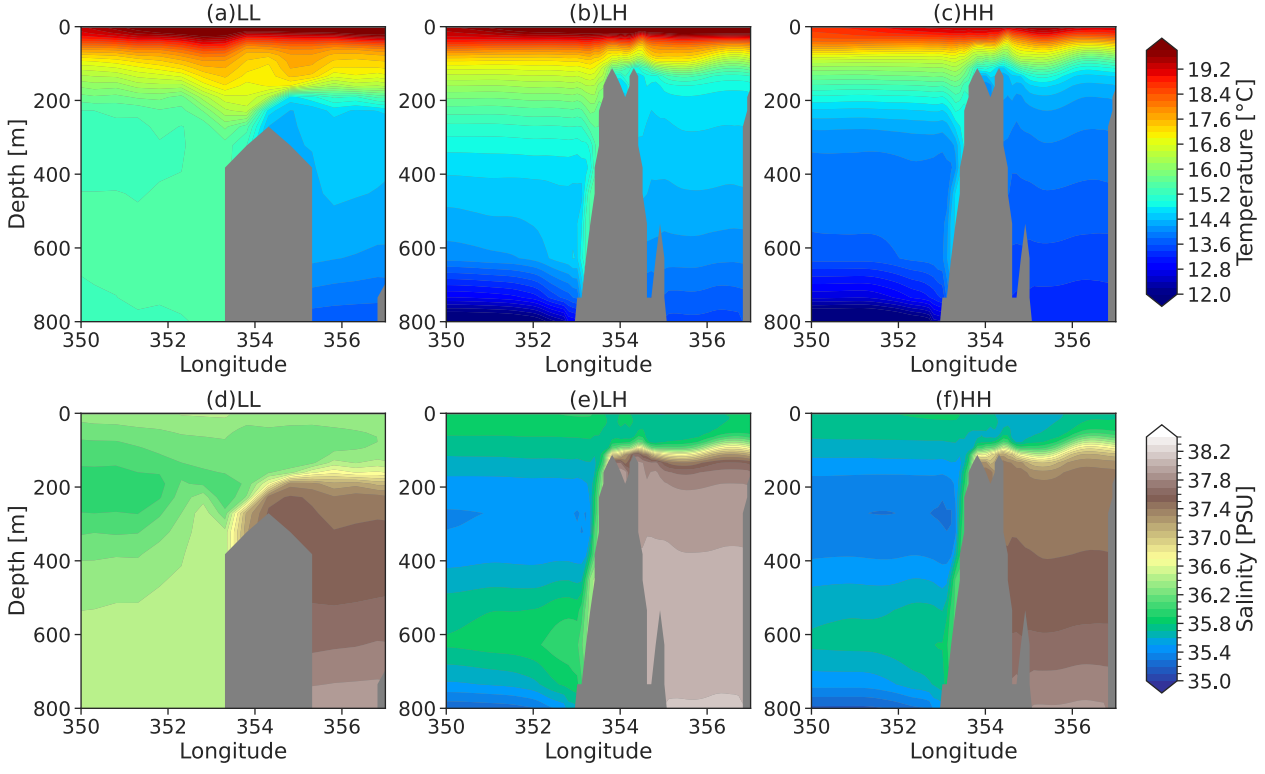

Figure A2. Vertical cross-section of annual mean temperature (°C) (a–c) and salinity (d–f) through the Strait of Gibraltar (36°N) (d–f) for all three simulations. The annual means are computed over simulations years 51–100.